Skin Tissue Terahertz Imaging for Fingerprint Biometrics

by

Peng Zheng

A Thesis Presented in Partial Fulfillment
of the Requirements for the Degree
Master of Science

Approved June 2017 by the
Graduate Supervisory Committee:

Georgios Trichopoulos, Chair
James Aberle
George Pan

ARIZONA STATE UNIVERSITY

August 2017

ABSTRACT

Fingerprints have been widely used as a practical method of biometrics authentication or identification with a significant level of security. However, several spoofing methods have been used in the last few years to bypass fingerprint scanners, thus compromising data security. The most common attacks occur by the use of fake fingerprint during image capturing. Imposters can build a fake fingerprint from a latent fingerprint left on items such as glasses, doorknobs, glossy paper, etc. Current mobile fingerprint scanning technology is incapable of differentiating real from artificial fingers made from gelatin molds and other materials. In this work, the adequacy of terahertz imaging was studied as an alternative fingerprint scanning technique that will enhance biometrics security by identifying superficial skin traits. Terahertz waves (0.1 – 10 THz) are a non-ionizing radiation with significant penetration depth in several non-metallic materials. Several finger skin features, such as valley depth and sweat ducts, can possibly be imaged by employing the necessary imaging topology. As such, two imaging approaches 1) using quasi-optical components and 2) using near-field probing were investigated. The numerical study is accomplished using a commercial Finite Element Method tool (ANSYS, HFSS) and several laboratory experiments are conducted to evaluate the imaging performance of the topologies. The study has shown that terahertz waves can provide high spatial resolution images of the skin undulations (valleys and ridges) and under certain conditions identify the sweat duct pattern.

TABLE OF CONTENTS

Page

LIST OF TABLES

Table Page

LIST OF FIGURES

Figure Page

Figure Page

Figure Page

Figure Page

Figure Page

Figure Page

Figure Page

CHAPTER 1

INTRODUCTION

This work introduces a new method for fingerprint imaging using Terahertz (THz) waves (300 GHz – 10 THz). We present numerical validation and experimental measurements, and indicate that THz imaging is a promising technique to be used for fingerprints identification. Fingerprints identification belongs to biometric identifier family which is often categorized by using physiological characteristics, such as fingerprints, voice, DNA, iris, and scent. Voice identification is convenient and high security. However, it uses massive resources to store the voice data. Iris scanning is a relatively new technology. The iris is an internal organ that is well protected against damage and wear by a highly transparent and sensitive membrane. The texture of iris remains remarkably stable over many decades.

Fingerprints are unique identifiers specific to each individual. It stops growing during embryonic gestation and does not change for the lifetime (Galton, 1892). Fingerprint identification requires a short time for enrollment and multiple algorithms have been employed to enhance the security. As one of the most widely used biometric identifiers, fingerprint imaging has been developed and explored by many predecessors.

1.1 The History of Fingerprints

1.1.1 First Reference of Fingerprint Use

The earliest prehistoric picture of a hand with fingerprint ridges was discovered on a Nova Scotia cliff as shown in figure 1.1(a). References from the era of the Babylonian king Hammurabi (1792-1750 B.C.) indicate that law officials fingerprinted people who had been arrested. Around 1900 B.C. in Babylon, to prevent falsification and

forgery, parties to a legal contract impressed their fingerprints into the clay tablet on the contract. From 221 B.C. to 220 A.D., in ancient China, the most popular application of fingerprint ridges was the clay seal. Ancient Chinese authors impressed their names on the front side of the clay and their fingerprints on the back side of the clay, which were used to give the document authenticity as shown in figure 1.1(b) (Xiang-Xin, 1988).

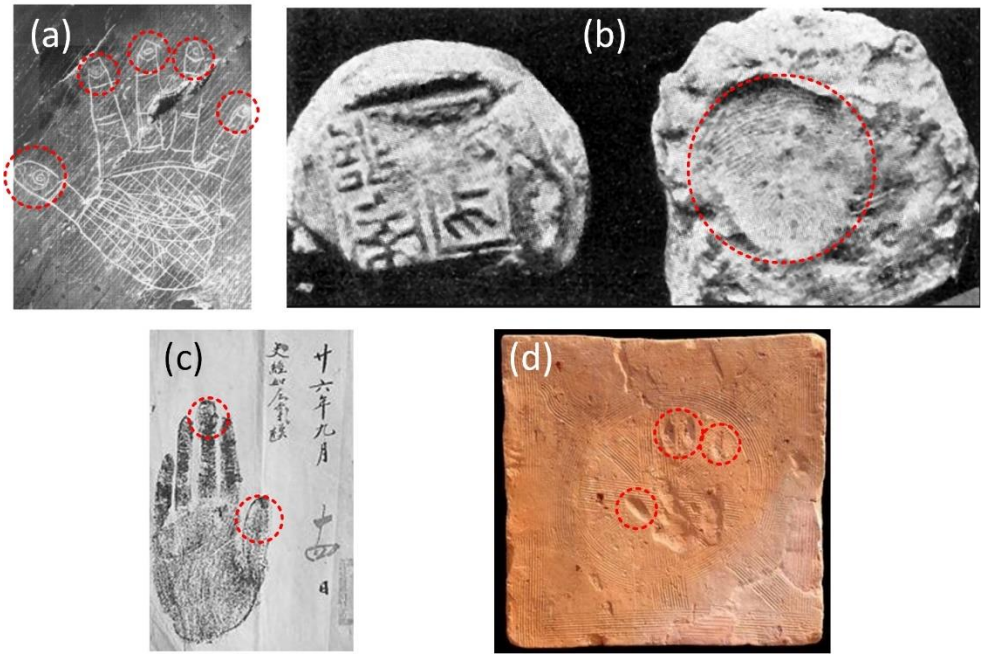

FIGURE 1.1: (a) The petroglyph found at Kejimkujik Lake, Nova Scotia. It can be dated before 1873 B.C. (adapted from Library - The History of Fingerprinting, 1998). (b) Fingerprints found on the backside of ancient Chinese clay as an identifying characteristic (adapted from MYTH OF FINGERPRINTS, 2009). (c) Fingerprints found on Chinese pottery and landscape painting. (d) Fingerprints found on an ancient Roman floor tile (adapted from BBC, 2003). Fingerprints are indicated by dash circles.

By 702 A.D., Japan adopted the Chinese practice of sealing contracts with fingerprints. According to the ancient Japanese domestic law, the people who could not write, they could hire other people to write for them, but they had to sign with their index fingerprint at the end of the document (Ashbaugh, 1999). This evidence shows that the ancient Japanese realized the identifying ability of the fingerprint at that period.

Fingerprints also have been found on Chinese pottery and landscape painting (Figure 1.1c) and tiles in Rome (Figure 1.1d). The evidences show that ancient civilizations realized the uniqueness and importance of fingerprints.

1.1.2 First Verification of Fingerprint Uniqueness

In the 14th century Persia, Hamadani commented that "experience shows that no two individuals have fingers exactly alike" based on the fact that Chinese people identified different people via their fingerprints. This is the earliest reference to fingerprints' uniqueness (National Institute of Justice, 2011). In the 17th century, European scientists began to publish their observations of fingerprints. The ridges, furrows, and pores on hand (as shown in figure 1.2) and foot surfaces were first described in detail by Dr. Nehemiah Grew in 1684 (Grew, 1684). Dr. Grew's paper marked the beginning in the western hemisphere of fingerprints observations and characterizations.

In 1686, Marcello Malpighi published an article which indicated the existence of patterns of ridges, spirals, loops and sweat gland in fingerprints and fingertips. Although fingerprint had been studied for several years, no one recognized the uniqueness of fingerprint until 1788 in Europe, when Johann Mayer wrote a book containing the

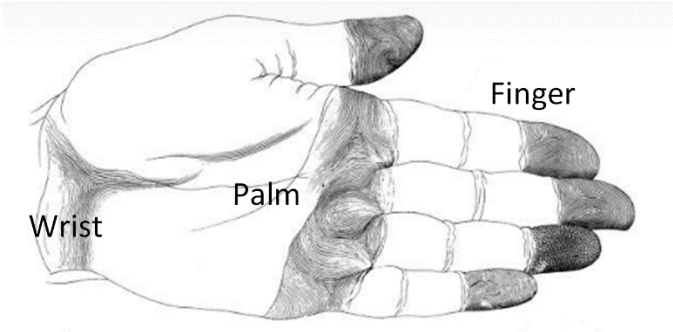

FIGURE (1.2): A picture of a human hand with ridges made by Nehemiah Grew. This marked the first fingerprint observation in the western hemisphere (adapted from Grew, 1684).

detailed drawings of friction ridge skin patterns. By mentioning that the arrangement of skin ridges is never duplicated in two persons, Mayer is considered the first person to recognize that fingerprints are unique (National Institute of Justice, 2011).

1.1.3 Fingerprints Become an Identification Tool

The English began using fingerprints is in July of 1858 when Sir William Herschel used fingerprints on native contracts (National Institute of Justice, 2011). In order to prevent a local man denying his signature in the future, Herschel made him put a handprint on the contract document as shown in figure 1.3a. This spontaneous printing is the first official use of friction ridge skin used by a European as a mean of authentication. Sir Francis Galton published the book, "Fingerprints" in 1892, discussing that fingerprint was unique and persistent. The book elaborated the first classification system for fingerprints. He discovered and scientifically proved that fingerprints do not change over the lifetime, and it is almost impossible for two fingerprints to be identical. According to his calculations, the odds of two exactly same individual fingerprints were 1 in 64 billion (Galton, 1892). In 1891, Juan Vucetich made the first criminal fingerprint identification based on recordings of criminal's fingerprints. He was able to identify a woman as the murderer by comparing her fingerprint with the fingerprint left on the crime scene as shown in figure 1.3b. The case is considered to be the first homicide solved by fingerprint evidence (National Institute of Justice, 2011).

FIGURE 1.3: (a) First official prints of hands and fingers made by W. J. Herschel (cited from *Prints of hands and fingers made by Herschel*). (b) Inked Fingerprints from the murder (adapted from The History of Fingerprints, 2017).

Sir Edward Richard Henry is best remembered today for his invention of the method of fingerprinting to identify criminals. Between July 1896 and February 1897, Henry invented a fingerprint classification system which enables fingerprint records to be organized and searched with relative ease. In 1924, the US established the Identification Division of the F.B.I. By 1946, the F.B.I. had successfully processed over 100 million fingerprint cards in manually maintained files and over 200 million cards by 1971. The files were split into computerized criminal files and manually maintained civil files, due to the developed of Automated Fingerprint Identification System (AFIS) technology (National Institute of Justice, 2011). Currently, paper fingerprint cards are not in use. Instead, new fingerprint scanners based on different technologies are more and more popular.

1.2 Current Fingerprint Scanning Technologies

Fingerprint scanners are not just reserved for the highly advanced devices these days, even the reasonably priced devices, e.g., cell phones and personal computers, are equipped with fingerprint scanners. This technology has evolved rapidly in the last decade. In this section, the three mainstream technologies are introduced and compared

including the optical fingerprint scanner, the capacitive fingerprint scanner, and the ultrasonic fingerprint scanner.

1.2.1 Optical Fingerprint Scanner

The optical fingerprint scanner is the most conventional method of capturing fingerprints. As suggested by the name, the technique relies on capturing the optical image of the user's fingerprint. A LED light source emits the light beam to the fingerprint surface through a prism, and then the fingerprints reflect the light beam and a lens focus the light beam to an image sensor, as shown in figure 1.4. After capturing the fingerprint, post-processing algorithms are employed to detect unique patterns on the surface, such as ridges and valleys through the analysis of the brightness of different areas in the image.

Same as the camera, the optical sensors have a wide range of resolution. With high resolution, many details can be discerned about the finger. The optical fingerprint scanner captures much higher contrast images compared to a regular camera since there is typically a large number of photodiodes in the scanner to capture the details. All the photodiodes are integrated into a sensor called Charge Coupled Device (CCD), which is the heart of the optical fingerprint scanner. CCD generates an electrical signal in response to the light photons. The optical fingerprint scanner is very popular due to its low cost. For example, optical fingerprint scanner products, such as the Microsoft Fingerprint Reader (Figure 1.5a) or the Arduino Fingerprint Reader (Figure 1.5b), have been used frequently in school for taking attendance (The Straits Times, 2017).

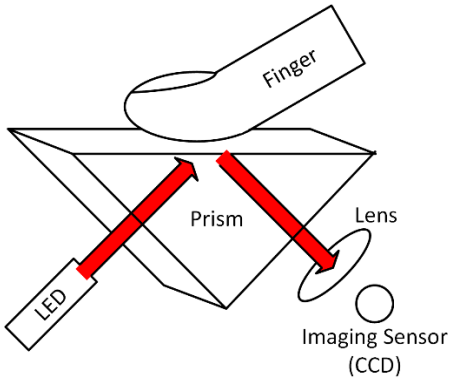

FIGURE 1.4: Optical fingerprint scanner schematic diagram: The light emits from the LED light source and projects on the fingerprint. The reflective light beam will be focused by the lens to the image sensor (CCD).

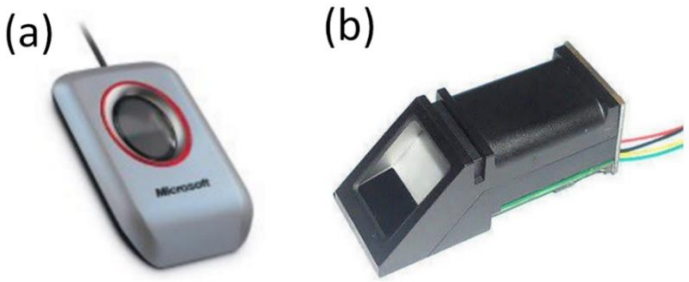

FIGURE 1.5: Optical fingerprint scanner products: (a) Microsoft Fingerprint Reader and (b) Arduino Fingerprint Reader.

The major drawback of the optical fingerprint scanners is the limited performance on security. As the technology is only capturing a 2D picture of the surface fingerprint, a counterfeit of the fingerprint picture can be used to deceive the system. Also, the scanning accuracy can be compromised by ambient light or skin dirt.

1.2.2 Capacitive Fingerprint Scanner

The most widely used type of fingerprint scanner today is the capacitive fingerprint scanner. Instead of directly capturing the image of a fingerprint, capacitive

fingerprint scanner uses capacitor array circuits to collect the characteristics of a fingerprint (Aditya Tiwari, 2016). Since capacitors can store electrical charge, the details of a fingerprint can be tracked by connecting them up to a conductive plate on the surface of the scanner as shown in figure 1.6. The picture shows the cross-section view of the scanner. Multiple capacitors are integrated into a plate and when a finger presses on the plate, then the sensor reads the corresponding capacitance. Ridges and valleys will cause a difference in the capacitance since there is air between the valley and plate, leading to an extra capacitance in the valley region compared to the ridge, which is directly contact with the sensor. An inverter and an operational amplifier integrator circuit are used to track these changes and create the analog signals. An analog-to-digital converter (ADC) is used to convert the analog signal to digital signal. The scanner processor will read the output digital voltage and determine whether it is a ridge or a valley. The processor can generate an overall picture of the fingerprint by reading every cell in the sensor array.

The main advantage of the capacitive scanner is that it requires a real fingerprint-type shape, rather than a photograph of a fingerprint, which enhances the system security. Additionally, by employing a semiconductor chip rather than a CCD unit, capacitive scanners tend to be more compact than optical scanners as shown in figure 1.7a.

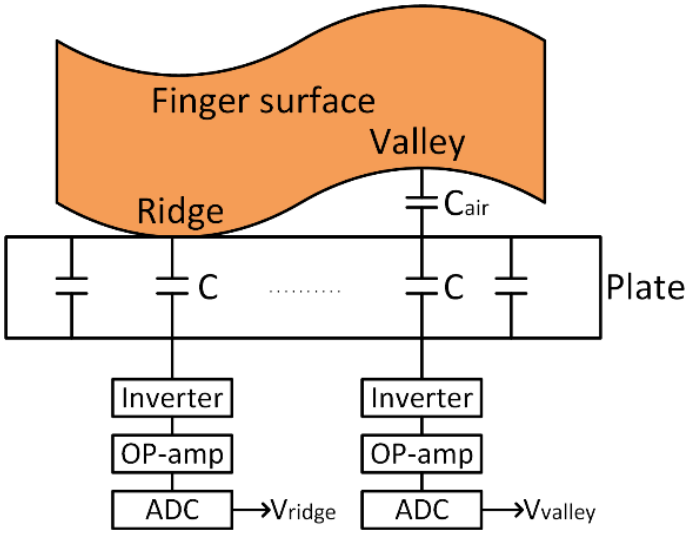

FIGURE 1.6 The theory and architecture behind a capacitive fingerprint scanning chip.

The most famous application of the capacitive fingerprint scanner is the "Touch ID" from Apple, Inc (Apple, 2015). The devices including iPhone 5s or later are packaged with Touch ID technology as shown in figure 1.7b. The steel ring can detect the touching of the finger, and then the scanner starts to capture the fingerprint. The thickness of the sensor is 170 um and the resolution is 500 pixel per inch. The sensor uses advanced capacitors to take a high-resolution image from a small section of a user's fingerprint. The sensor can categorize the fingerprint to three basic types, which are arch, loop, or whorl. It also maps out details in the ridges that are undetectable by the human eye and even detects minor variations in ridge direction caused by pores and edge structures.

The drawback of the capacitive fingerprint scanner is that it can be deceived by a mold of a person's finger. Since the capacitive fingerprint scanner depends on users fingerprint undulation (ridges and valleys), a counterfeit finger with the same fingerprint undulation (ridges and valleys) can deceive the scanner.

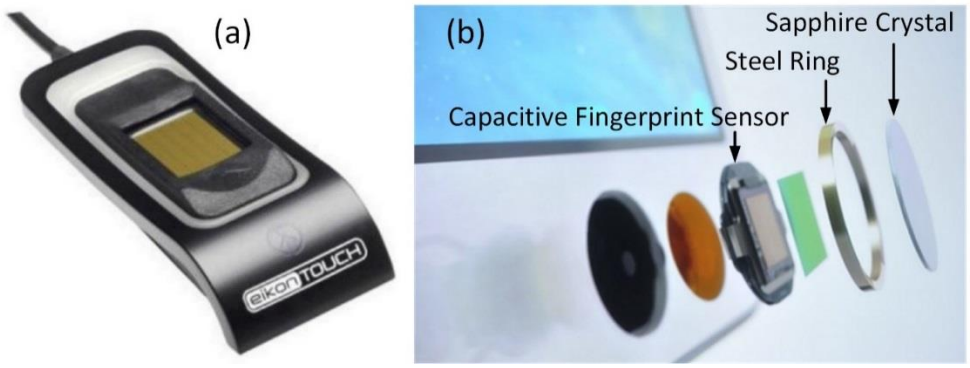

FIGURE 1.7: (a) Digital Persona Eikon Touch 710 Fingerprint Reader with capacitive fingerprint scanning chip. (b) Components of the capacitive fingerprint scanner used in Iphone5s. (adapted from Apple, 2015)

1.2.3 Ultrasonic Fingerprint Scanners

Ultrasonic fingerprint scanners exploit the principles of medical ultrasonography to create visual images of the fingerprint. To capture the details, the hardware consists of both an ultrasonic transmitter and a receiver using piezoelectric materials (Robert Triggs, 2016). The ultrasonic waves are transmitted toward the finger placed over the scanner as shown in figure 1.8. Some of the waves are absorbed in the dermal skin layer while some are reflected back to the sensor, depending on the ridges, pores, and other traits that are unique to each fingerprint. At different points on the scanner, the intensity of the returning ultrasonic waves can be captured and calculated by the sensor, which results in a detailed 3D reproduction of the scanned fingerprint. Scanning for a longer period allows for additional depth data to be captured. As such, the 3D fingerprint images of this capture technique improves security compared to capacitive and optical scanners.

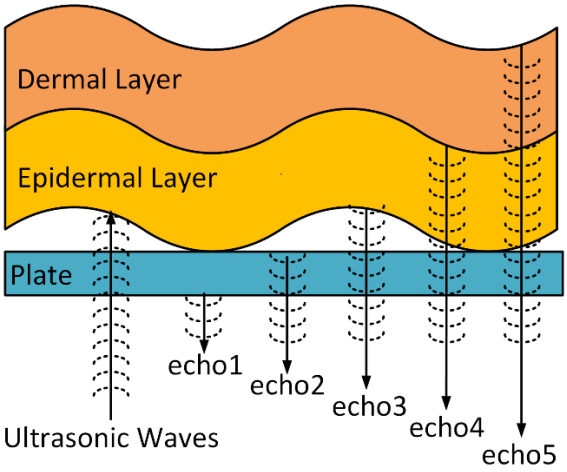

FIGURE 1.8: Ultrasonic fingerprint scanner working theory. Ultrasonic waves transmit to fingerprints, different layers will reflect different waves.

The advantage of the ultrasonic fingerprint scanner is higher security performance, because ultrasonic fingerprint scanner can get the inner layer undulation information. In 2016, Hao-Yen Tang proposed a 3D ultrasonic fingerprint sensor using ultrasonic transducers as the signal source which is working at 14MHz (Tang, H., 2016). The results shown in figure 1.9 indicate that the proposed sensor can effectively distinguish ridges and valleys both on the epidermal layer and dermal layer even when wet.

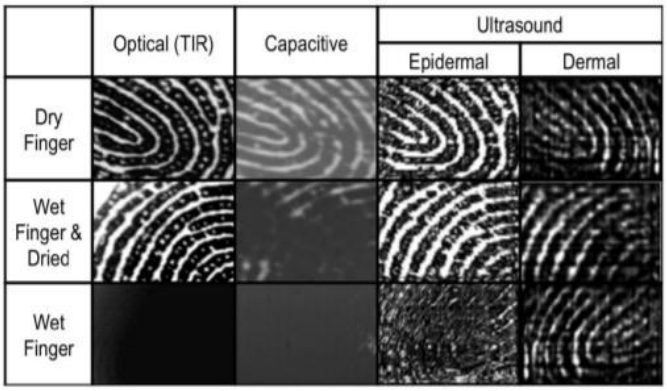

FIGURE 1.9: Fingerprints captured by commercial optical and capacitive fingerprint sensors compared with the ones captured by the proposed

ultrasound fingerprint sensor under different conditions of finger wetness. (cited from Tang, H., 2016)

The ultrasonic fingerprint scanner is still immature and has not been widely employed in practice. Additionally, when compared to the proposed method which will be discussed in Chapter 3 and Chapter 4, the ultrasonic fingerprint scanner cannot detect the sweat ducts information.

1.3 Threats of Fake Fingerprints

The extensive use of fingerprints for identification motivates imposters to fabricate counterfeit fingerprints. For the first time, the FBI identified a forgery by a law enforcement officer in 1925 (Waller, 2002). In 1998 Willis and Lee successfully produced the artificial fingerprints that can deceive multiple finger scanners (Meyer, 1998). They studied the scanners from six corporations. All of the scanners offer optical techniques that capture a fingerprint image, using a light source refracted through a prism. Due to different structures and the working theory behind these devices, only two of them were able to detect the fake fingerprints by combining optical and proprietary finger-detection methods.

In 2000 Van der Putte and Keuning systematically studied a number of fingerprint scanners and made several dummy fingers from silicon rubber and other materials (Putte, 2000). They deceived four optical sensor scanners and two silicon-based capacitance sensor scanners. After the testing, they concluded that the fingerprint scanners currently could not accurately differentiate between real, living fingers and a dummy fingers. In 2001, Kakona described how to spoof an optical fingerprint sensor using a printed fingerprint (as shown in figure 1.10) and reactivating latent fingerprints on the sensor's surface by breathing on it (Li, 2009). In 2002, Matsumoto described procedures of

making artificial fingers from gelatin silicon and gummy molds (Matsumoto, 2002). Their experimental results showed that gummy fingers can deceive all eleven tested fingerprint scanners.

FIGURE 1.10: Printed fingerprinte spoofs an optical sensor.
Cited from (cited from Li, 2009).

The failure of fingerprint scanners to detect counterfeit fingerprints raised serious concerns in the biometrics community. In recent decades, many researchers proposed various methods to approach this problem. In 2001, Derakhshani proposed a purely software based method by detecting the perspiration process from two consecutive fingerprints captured during 5 seconds as shown in figure 1.11, since the perspiration process does occur for a phantom (Derakhshani, 2003). Classification is performed using a back propagation neural network trained by example fingerprints. This setup quantifies the sweating pattern and makes the final decision on the vitality of the fingerprint.

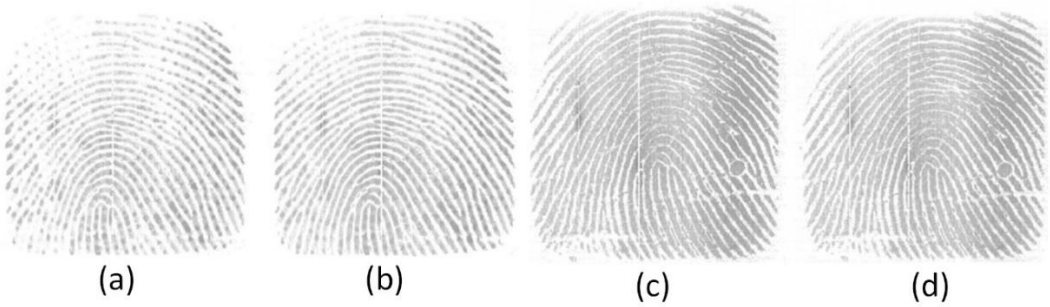

FIGURE 1.11: A live finger first scan (a) and last (five seconds later) scan (b). A phantom finger first scan (c) and last scan (d). Due to the perspiration process in a live finger, the fingerprint in (b) is clearer than (a). Since perspiration process doesn't occur in a phantom finger, (c) and (d) are the same (cited from Derakhshani, 2003).

In 2007, Jia and Cai proposed a "Support Vector Machine" based method to differentiate fake fingerprints from real ones (Jia, 2007). This method analyzes a time-series of gradually deformed fingerprints and extracts two static features related to perspiration and three dynamic features related to skin elasticity. They also proposed 5-tuple features representing the skin elasticity and the physiological process of perspiration. The features had strong efficacy in discriminating the fake fingers from real ones and high adaptability to the variations in skin conditions. The experimental results showed that the proposed features and approach are effective in fake finger detection.

In 2012, Galbally proposed a detection method based on ten quality features, which are related to ridge strength, ridge continuity, and ridge clarity (Galbally, 2012). The method correctly classified almost 90% of the fingerprint images. This proves its ability to adapt to all types of direct attacks and its efficiency as a method to enhance the general security capability of fingerprint verification systems.

All the approaches to enhance the security are based on software enhancement or combined with finger physical characteristic, such as perspiration. However, the post-processing of the sensory data cannot ultimately solve the problem induced by the limited performance of the scanners mentioned above. We are trying to design a new fingerprint imaging technology that by using THz waves to image the fingerprint, the sweat ducts image is combined with ridges and valleys images to enhance the security level. THz waves have smaller wavelengths when compared to microwaves. This feature allows the

capture of high spatial resolution images. Another advantage is that THz waves can penetrate human surface tissue in near-field; but unlike the X-rays, THz waves are not harmful to human body. In the following chapter, we describe the useful properties if THz imaging that can be applied in fingerprint scanning for enhancing security and accuracy.

CHAPTER 2

THZ IMAGING APPLICATIONS AND HUMAN FINGERPRINT PROPERTY

THz radiation can penetrate various materials, such as clothing, paper, plastic, and ceramics, making it a useful tool in various sensing and imaging applications. For example, it could be used as a replacement for medical X-rays in the near-field case due to the unharmful property of THz. This chapter is split into three sections: the first section includes some applications of the penetrating ability of THz radiation; the second section specifically describes the THz imaging application on human tissue; the third section discusses the property of the fingerprint.

2.1 THz Waves Non-destructive Imaging Applications

The first THz imaging application was in 1995, from B. B. Hu and M. C. Nuss, AT&T Bell Laboratories (Hu, B. B., 1995). They demonstrated a novel chemical imaging

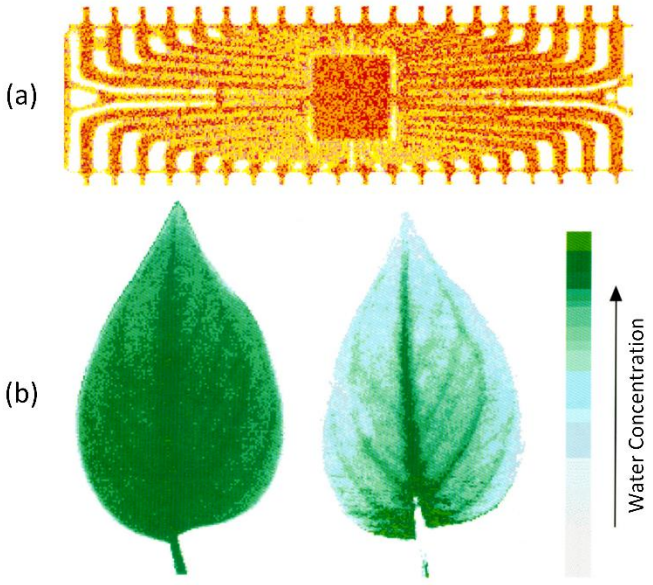

FIGURE 2.1: (a) THz image of a packaged semiconductor integrated circuit with plastic packaging (cited from Hu, B. B., 1995). (b) THz image of a leaf when it is fresh and 48 hours later (cited from Hu, B. B., 1995).

system based on optoelectronic THz time-domain spectroscopy (THz-TDS). A packaged semiconductor and a leaf were imaged by the imaging system as shown in figure 2.1ab. The image of packaged semiconductor verified the penetration ability of THz waves. The image of the leaf indicated that the THz waves were sensitive to the density of water, which showed the opportunity for water detection.

In 2002, Bradley Ferguson and his colleagues demonstrated a tomographic imaging approach that uses pulsed THz radiation to probe the optical properties of 3D structures in the far-infrared (Ferguson, 2002). Figure 2.2(a) shows an optical photograph

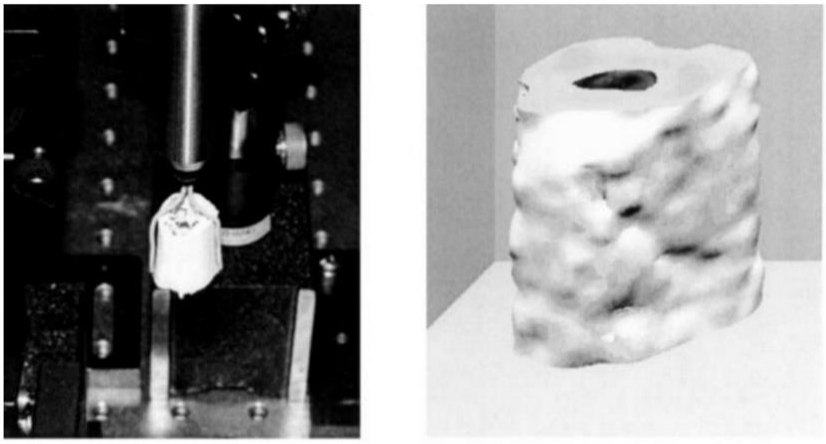

FIGURE 2.2: A piece of turkey bone was imaged with the T-ray CT system. The fine structure inside the bone is of the order of the THz wavelength and therefore causes difficulties in reconstruction. (a) Optical image. The turkey bone was reconstructed, and (b) a 3D rendered image was generated. The reconstruction used the amplitude of the THz pulses at each pixel as the input to the filtered back projection algorithm (cited from Bradley, 2002).

of the target: a piece of turkey bone. This sample was imaged with the THz computed tomography (CT) system, and the bone image is reconstructed by the amplitude of the measured THz pulses as shown in figure 2.2(b).

In 2005, Nicholas Karpowicz and his colleagues reported the use of a compact continuous-wave sub-THz system for inspection applications (Karpowicz, 2005). They did two scanning experiments with a standard size briefcase. The case is empty in the first experiment but in the second experiment, the bag contains benign and suspicious items. The results (as shown in figure 2.3) clearly show the knife in the second case, indicating the opportunity for the potential applications in security scanning.

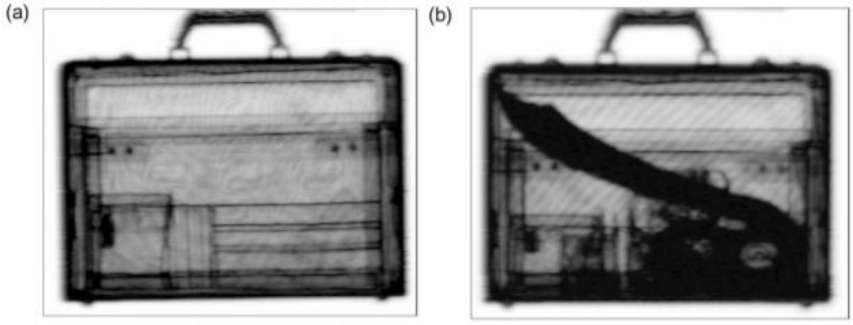

FIGURE 2.3: (a) The THz Pulse Image of an empty briefcase. (b) The THz Pulse Image of a briefcase with a knife (cited from Karpowicz, 2005).

In 2007, X-C Zhang presented the THz image of a teapot as shown in figure 2.4. The water inside the teapot is obvious in the image as shown to be the dark part. This is because water exhibits strong absorption of the THz waves (Hu, Q, 2008).

FIGURE 2.4: The image of a teapot by using Gunn diode and a Schottky diode detector at 200 GHz. The upper image is the photograph for the teapot. The image on the left bottom is the THz image without water inside and the one on the right is with the water inside (cited from Hu, Q, 2008).

In 2011, Goutam Chattopadhyay and his colleagues presented a 675 GHz imaging radar which can generate a concealed objects image through volunteer's clothes in the NASA Jet Propulsion Laboratory (Cooper, 2011). The images as shown in figure 2.5 present that the wave penetrated the volunteer's jacket to capture the image of the pipes.

In the meantime, significant progress has been achieved in multipixel sensing systems. In 2015, the first THz camera was manufactured (Trichopoulos, 2015), shown in figure 2.6, which operates in the 0.6–1.2 THz band with a five frames-per-second image acquisition speed. The camera sensor consists of broadband THz antennas monolithically integrated with ultra-fast heterostructure backward diodes as shown in figure 2.6a. The image results indicate that the THz camera can be used in the different imaging applications, such as security screening.

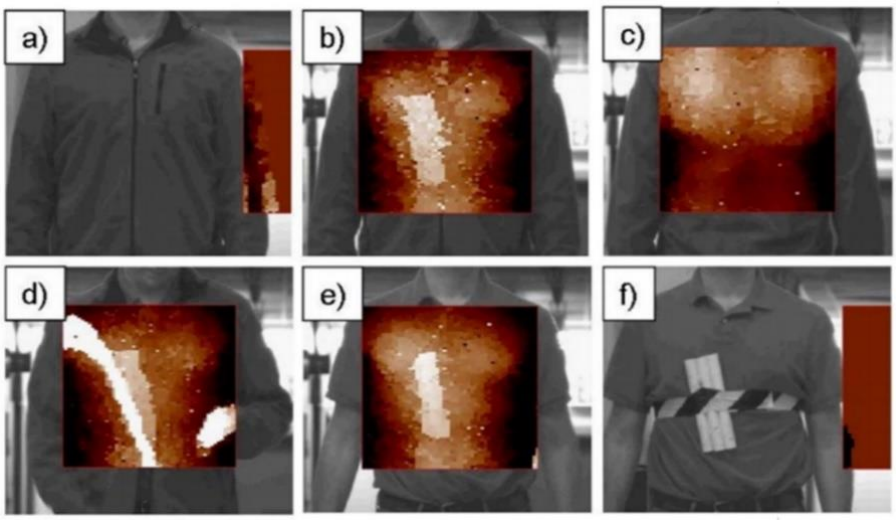

FIGURE 2.5: Six radar images captured by a 1-Hz frame rate real-time radar imager. Visibly, there is no evidence of three 1-in PVC pipes concealed by a jacket (a). The pipes are visible when the subject moves into the radar field of view (b). No hidden objects are detected on the subject's back (c). Some image streaking (d) is a consequence of not running at video rates. With no jacket, the pipes are detected both in the radar image (e) and visibly (f) (cited from Cooper, 2011).

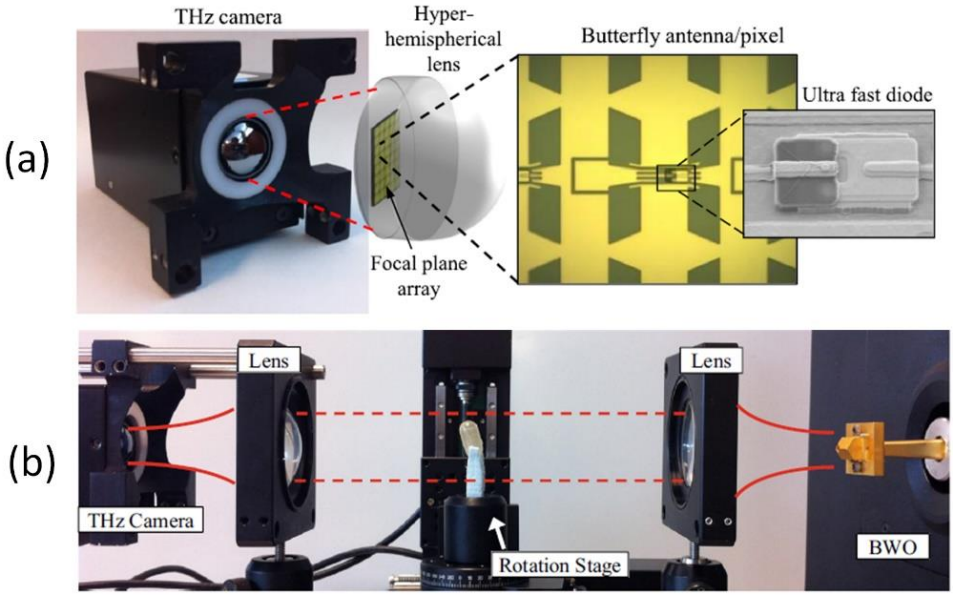

FIGURE 2.6: (a) The THz camera: the focal plane array is located behind a hyper-hemispherical silicon lens and planar wideband antennas integrated with ultra-fast diodes form the THz imaging array. (b) View of the reverse microscope configuration setup for THz computed tomography. As the object in the middle is rotated, the THz camera collects the projected images at multiple angles for CT reconstruction (cited from Trichopoulos, 2015).

2.2 THz Imaging Applications on Biological Tissue

In 2001, Bryan E. Cole demonstrated the application of THz pulse imaging for the in-vivo study of the upper layers of the human skin. A THz signal pulse is used to probe the skin in a manner similar to the ultrasonic fingerprint scanner. The incident pulse is reflected by spatial changes in either the refractive index or absorption coefficient of the skin tissue and the time-of-flight for the detection of the reflected pulse provides the depth information on the scattering center. They mapped the thickness and the hydration level of the stratum corneum. As shown in figure 2.7a, the peak amplitude of the THz

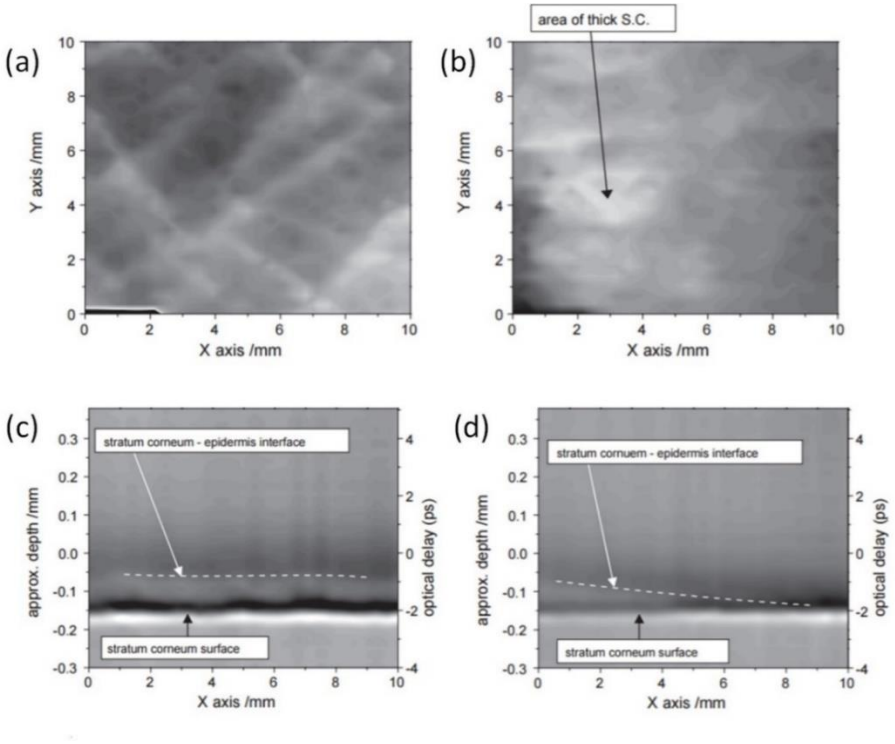

FIGURE 2.7: (a) An image over the 1cm x 1cm raster scanned area of the side of the subject's hand, generated from the peak value of the processed THz waveform corresponding to the outside surface of the stratum cornea. The topographic features of the skin surface (lines, wrinkles etc.) are evident. (b) An image generated from the same dataset but with the THz waveform values at a time delay corresponding to the stratum cornea-epidermis interface plotted. In this case, variations in the S.C. thickness over the scanned area are highlighted. (c) A slice through a 3D data set of an area on the central portion of the subject's palm. The grey-scale indicates the THz

amplitude and is plotted against optical delay (vertical axis) and x-position across the scanned area (horizontal axis). The stratum cornea top surface and epidermis interfaces are indicated. (d) A similar plot from a dataset obtained on the edge of the subject's hand; the decrease in stratum cornea thickness across the x-axis is evident (cited from Bryan, 2001).

wave is plotted and the surface variations in the skin topology are evident as lines/wrinkles. Figure 2.7b is plotted by selecting the higher optical delay value which corresponds to the stratum corneum-epidermal layer interface. The figure 2.7c and 2.7d are cross-section images to display the objects depth profile versus position along a line, however for different hand area. The vertical axes represent the optical delay value and it has been converted to approximate depth in the skin. The stratum corneum top surface and epidermis interfaces are indicated (Bryan, 2001).

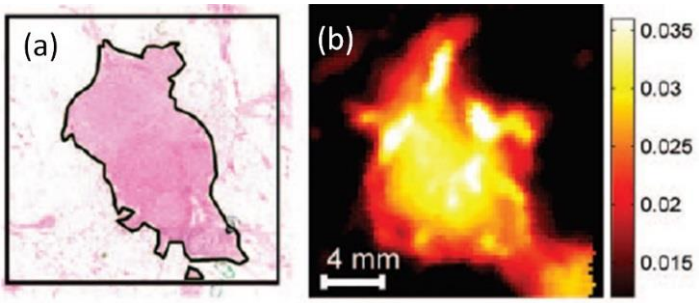

FIGURE 2.8: (a) Photomicrograph and (b) THz image for invasive ductal carcinoma illustrate the method to compare shapes of tumor regions (cited from Fitzgerald, 2006).

In 2006, Fitzgerald and his colleagues performed THz pulse imaging (TPI) experiments for human breast tumors (Fitzgerald, 2006). The THz image obtained by THz time-domain spectroscopy (THz-TDS) technique shows the distinct structural organization with different zones. As shown in figure 2.8, the result clearly distinguished between the normal and abnormal breast tissues based on the fact that the normal tissue absorbs THz wave while tumor tissue reflects the THz wave.

In 2012, Zachary D. Taylor and his colleagues used a THz imaging system to acquire high-resolution images of deep and partial thickness burns for a live rat (Tewari, 2012). THz imaging is highly sensitive to water concentration and relative robustness to surface scatter. Figure 2.9a shows the photograph of abdomen skin without injury and figure 2.9b shows the photograph of injured skin after 7 hours. The THz imaging results are figure 2.9cdef, split by the burning time from 0 to 7 hours, respectively.

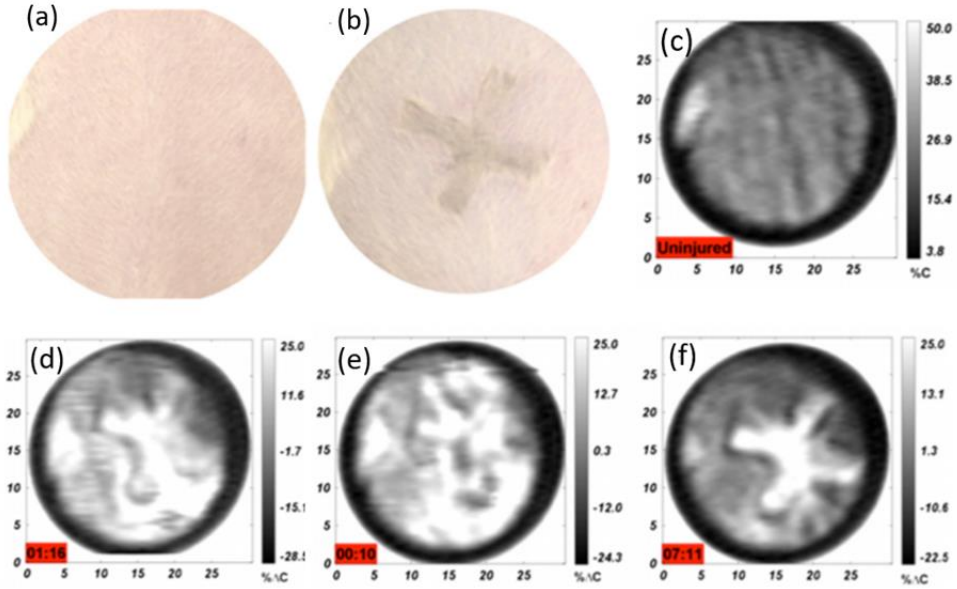

FIGURE 2.9: (a) Photograph of skin without injury and (b) with injury. (c-f) The THz images for injury area from 0 to 7 hours, respectively (cited from Zachary, 2012).

Therefore, THz waves propagation and scattering can be dramatically affected by the material or tissue electrical properties, leading to the intensity difference in reflective waves. In order to study the viability of THz imaging technology in fingerprint scanning, the properties of finger tissue need to be discussed as follows.

2.3 Can THz Waves Reveal the Subcutaneous Morphology of the Finger Skin?

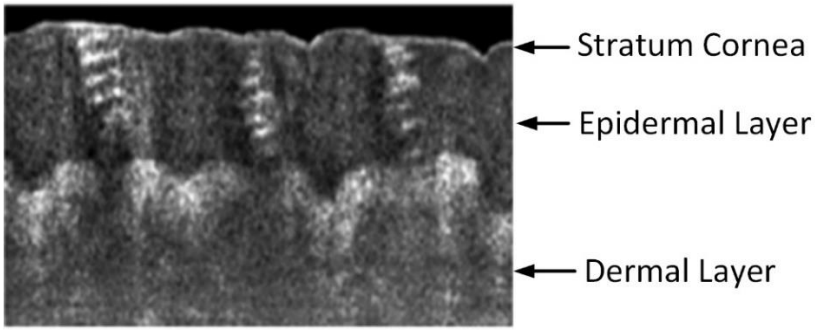

Figure 2.10 The Optical coherent tomography imaging of the human skin (cited from Hayut, 2013).

The finger skin can be split into main three layers, stratum corneum, epidermal layer, and dermal layer as shown in figure 2.10. The sweat ducts inside the epidermal layer has a helical geometry. Since the thickness of the stratum corneum is around 50um (Hayut, 2013), which is very thin compared to the thickness of the epidermal layer, the stratum corneum is ignored in this study for simplification reasons. The undulation of the epidermal layer is around 50um and 100um for the dermal layer respectively, as

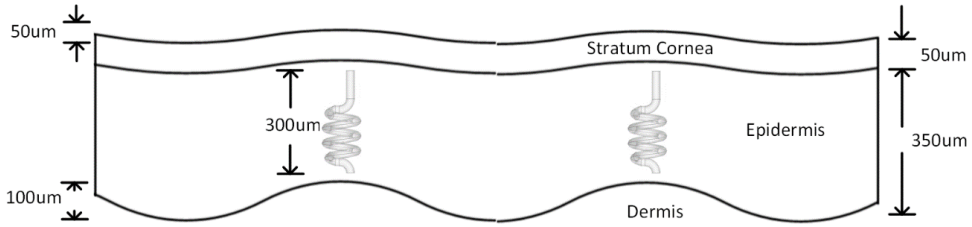

Figure 2.11 A simplified diagram of the finger surface. The thickness of different layers and sweat duct is labeled.

shown in figure 2.11. The conductivity of sweat ducts ranges from 100 to 10,000 S/m (Siemens/meter) while the conductivity is only 1 S/m for the epidermal layer and 30 S/m for the dermal layer (Hayut, 2013). The model parameters are summarized in Table I.

	Stratum cornea	Epidermis	Dermis	Sweat Duct
Dielectric Constant	2.4	3.8	3.9	4
AC Conductivity (S/m)	10^{-5}	1	30	100~10000
Thickness (um)	50	350	>1000	300

Table 2.1 Tissue property summary.

The sweat duct has a helical structure and due to the increased conductivity of sweat, it can be modeled as a lossy THz helical antenna. Due to the difference in geometry, the reflected signals from sweat ducts and surrounding tissue will be different. Also, the difference in the dielectric constant and conductivity between sweat ducts and the surrounding tissue will enhance the difference in the reflected signals. By detecting the location of the sweat ducts in fingerprint scanning, the security performance of the scanning will be improved. Thus, the helical structure of the sweat duct (as shown in figure 2.12) plays a significant role in our imaging system. According to (Balanis, 2016), the mathematic formula for the helical antenna resonant frequency is given by

$$f = \frac{c}{D \times \pi \times \sqrt{\epsilon_r}} \quad (2.1)$$

where c is light speed, D is the diameter of the duct, ϵ_r is the dielectric constant of the surrounding tissue. We assumed the diameter D is 100um, ϵ_r is 3.8 (epidermis), from the calculation, then the resonant frequency approxmately from 300 GHz to 500 GHz. This result matched with the result in (Tripathi, 2015).

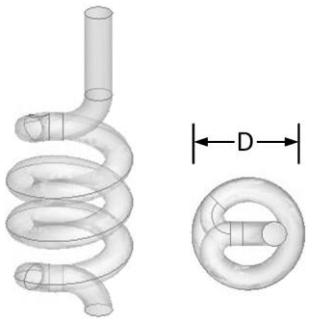

Figure 2.12 Helical antenna structure

side view and top view.

Current research has shown reasonable THz wave penetration depth and high spatial resolution capabilities. Also, human finger skin appears to have interesting electrical properties that we can be exploited to develop a novel fingerprint imaging techniques. In this work, we are interested in examining THz waves capability to image fingerprint undulations (ridges and valleys) and sweat ducts.

CHAPTER 3

SUBCUTANEOUS THZ IMAGING USING QUASI-OPTICS

To achieve accurate fingerprint scanning, we investigate two topologies: quasi-optical setup and near-field probing using THz antennas. This chapter presents the numerical validation of the quasi-optical setup and the experimental measurements. Optical components, such as mirrors and lenses, are used to focus THz waves onto a small spot on the skin and achieve high spatial resolution. Focusing components are very useful in reshaping the beam and coupling it efficiently on THz horn antennas that are integrated with ultra-fast detectors. Several THz imaging systems, raster scanning (Palka, 2015) or focal plane array based (Trichopoulos, 2015), rely on the use of optics. However, as opposed to the visible light, certain phenomena, such as diffraction, occur and have to be properly anticipated in the imaging system design.

3.1 Quasi-Optics

Quasi-optics refers to the propagation of a beam that is reasonably collimated but has relatively small dimensions when measured in wavelengths, as shown in figure 3.1. Quasi-optics cover a wide range of situations of practical importance in the design of systems, spanning from the microwave to submillimeter wavelength ranges. This contrasts with the geometrical optics, which deals with radiation in the limit that the wavelength equals zero. In other words, in geometrical optics, all the components are large enough when compared to the wavelength. However, when the wavelength is comparable to the system's dimensions, the diffraction effects and beam divergence become significant. The need of quasi-optics occurs when the radiating and optical aperture dimensions are comparable to the wavelengths, which allows the elegant theory

of Gaussian beam modes and Gaussian beam propagation to be employed (Goldsmith, 1998). The efficacy of Gaussian beam analysis is increased when feed horns are used as sources. Especially, in diagonal horn antennas, which are extensively used on mmW and THz waves, around 85% of the EM power is radiated into the fundamental Gaussian mode.

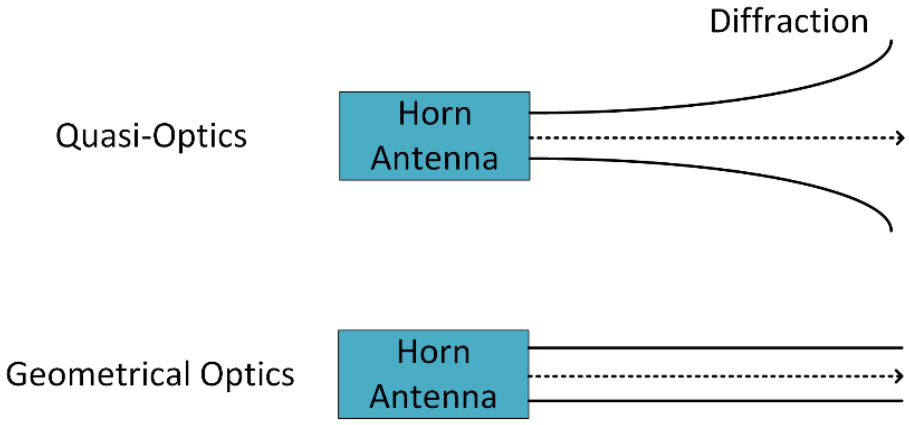

Figure 3.1 Quasi-optics waveform compares to geometrical optics waveform.

According to Fundamentals of Photonics (Saleh, 2007), the fundamental Gaussian beam complex electric field amplitude at a distance z is,

$$U(r,z) = A_0 \frac{W_0}{W(z)} exp\left[-\frac{r^2}{W^2(z)}\right] exp\left[-jkz - jk\frac{r^2}{2R(z)} + j\tan^{-1}\frac{z}{z_0}\right] \quad (3.1)$$

where,

$$W(z) = W_0\sqrt{1+\left(\frac{z}{z_0}\right)^2} \quad (3.2)$$

$$R(z) = z\left[1+\left(\frac{z}{z_0}\right)^2\right] \quad (3.3)$$

$$W_0 = \sqrt{\frac{\lambda z_0}{\pi}} \quad (3.4)$$

As shown in figure 3.2, r is the radial distance from the center axis of the beam, and z is the axial distance from the center axis of the beam. z_0 is known as the Rayleigh range. A_0 is the electric field amplitude when z=0. $W(z)$ is given by (3.2) and it is the beam waist at a distance z. W_0 is given by (3.4) and it is the beam waist when z=0. $R(z)$ is given by (3.3) and it is the radius of curvature of the beam's waveform at a distance z.

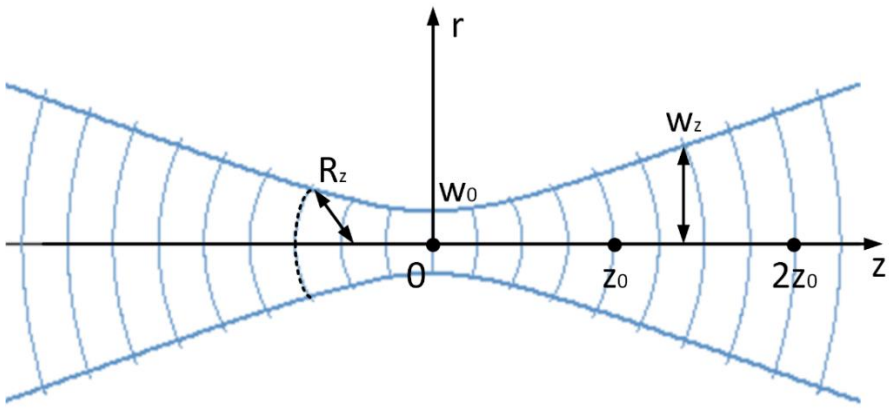

Figure 3.2 Waveform of a Gaussian beam.

3.2 Gaussian Beam Numerical Validation and Results Using Approximate Skin Models

In this section, we examine a simple, raster scanning topology that is based on the use of a highly focused THz beam to reconstruct the skin features of the finger. The THz scanner topology is shown in Fig. 3.4a. The necessary optics are used to form tightly focused beam on the focal point of a hemispherical silicon lens. For example, when the hemespherical lens is illuminated with a plane wave (or a collimated beam), the THz signal is focused on the focal point of the lens located approximately 0.39*R from the center of the lens (R is the lens radius) (Trichopoulos, 2010). As such, a silicon extender slab is needed to reach the focal point. By placing the finger skin on top of the silicon extender, a tightly focused spot is formed on the skin. Therefore, when the beam is

mechanically scanning the finger, a THz skin image of high spatial resolution is formed by recording the reflected signal from the transceiver. To investigate the THz wave-skin interaction under this imaging topology we first conducted a numerical analysis using a commercial finite element method EM field solver (ANSYS, HFSS).

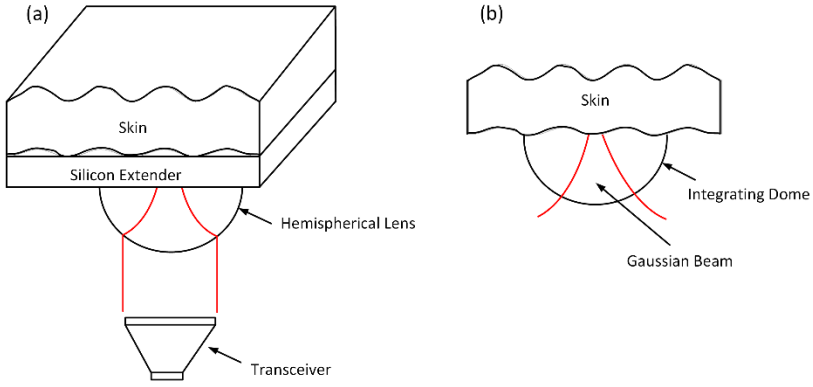

Figure 3.4 (a) Gaussian beam formation in the raster scanning imaging system using optics. (b) The schematic diagram after simplification for saving time.

To simplify the theoretical analysis we assume that the focused beam can be considered to have the same characteristics of a fundamental Gaussian beam. The computed image is now formed by calculating the total beam power that is crossing a specified surface on the model. As depicted in Fig. 3.4b, we define a dome-shaped volume around the focal point and use HFSS's Gaussian beam excitation to model the beam forming characteristics of the optical system. The spherical part of the dome is assigned to absorbing radiation boundaries to ensure that to signal is reflected back to the skin. The total power *P* (equation 3.6) is computed by integrating the Poynting vector *S* (equation 3.5) on the dome outer surface.

$$S = \frac{1}{2} Re[E \times H^*] \quad (3.5)$$

$$P = \iint_S S \cdot ds \quad (3.6)$$

The integration of the Poynting vector over the plane surface represent the summation of the incident and reflected beam power. To form the 2D THz image, the dome is displaced to several points across the skin model and the total power *P* is computed for every location.

The HFSS simulation model is shown in figure 3.5 at different angles. The grey rectangle with undulations represents the epidermis layer. The blue helical ducts correspond to sweat ducts. To simulate the actual situation when a person touches the fingerprint scanner, the top part of the undulations (ridges) is flattened, as shown in figure 3.5c. The ducts are uniformly distributed inside the epidermis. However different number of turns are intentionally set for the neighbor ducts. For example, in figure 3.5a, the ducts are either two turns or four turns. Some assumptions are made to simplify the simulation—1) the stratum corneum is ignored since its thickness is only 50um (Hayut, 2013); 2) the undulations for the epidermal layer and dermal layer are considered to be the same; and 3) dermal layer is represented by the finite conductivity boundary. The

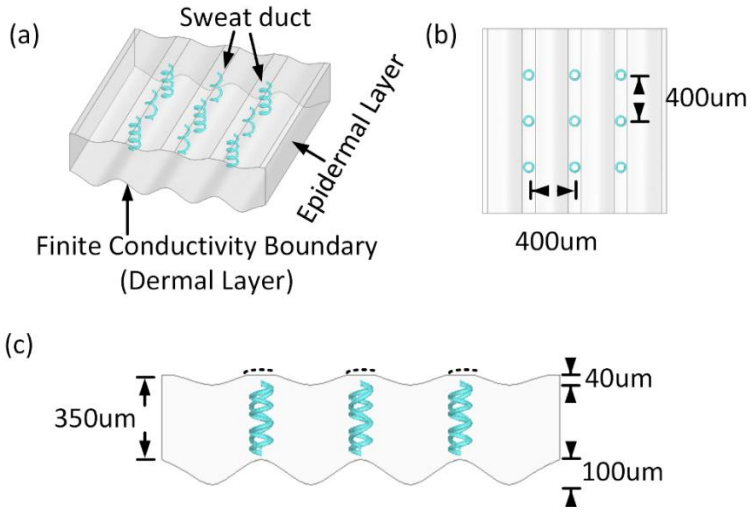

Figure 3.5 HFSS simulation model 3D view (a), top view (b), and side view (c).

properties of the epidermal layer, the dermal layer, and the sweat ducts are based on Table 1. The geometrical details are marked in figure 3.2b and 3.2c.

To further simplify the simulation to save simulation time, a cylinder with the same diameter as the dome intersects with the epidermal layer, which means only the epidermal layer and sweat ducts inside the cylinder are considered in the simulation, as shown in figure 3.6. We assumed the cylindrical domain is wide enough that the surrounding tissue will not contribute to the reflected power. Thus, the outer surfaces of the cylindrical domain are assigned absorbing boundary conditions, as shown in figure 3.6. During the simulation, the beam source, the dome, and the cylinder are both shifted with the same step. For each movement, the Poynting vector, which is the integration of the total electric field cross product total magnetic field over the dome, is used to represent the total power. The image of the fingerprint can be generated by plotting the total power versus their corresponding locations.

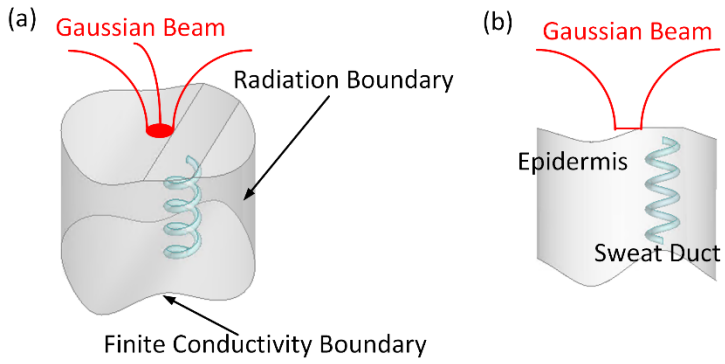

Figure 3.6 3D view (a) and side view (b) of the simplified simulation model. During the simulation, different parts of the tissue (epidermis and sweat ducts) will intersect with the shifting cylinder to achieve the raster scanning.

Figure 3.7 shows the image results with and without sweat ducts. The ridges, valleys, and sweat ducts are successfully detected as expected, which are marked in

figure 3.7a and 3.7b. The magnitude is normalized to 0dB. With the same geometry, the 4-turn duct image is slightly darker than the 2-turn duct image as shown in figure 3.7a, which indicates that more signal (energy) is absorbed when the duct has more turns.

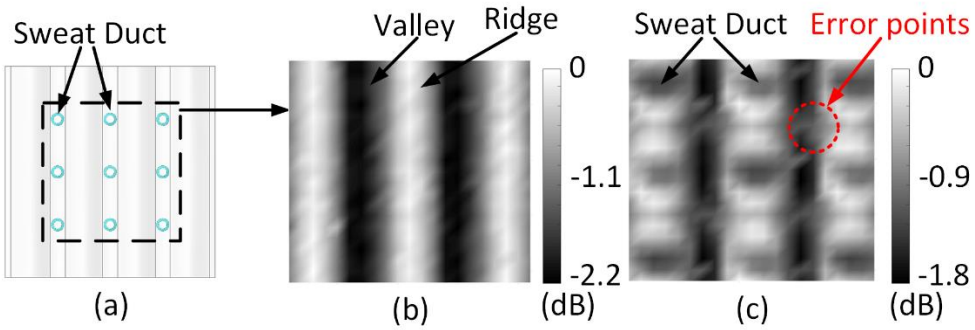

Figure 3.7 HFSS simulation model top view (a) and image on 490GHz with (b) and without (c) sweat ducts. Both ridges, valleys, sweat ducts are detected. The magnitude is normalized to 0 dB. Red dashed circles are error points.

During the simulation, when shifting the cylinder under the dome, the cylinder intersects with the epidermis and the ducts. HFSS mesh synthesis may fail when the geometry inside the cylinder is too complex. For example, when the cylinder intersects the duct, part of the duct will be maintained in the cylinder, and the rest of the duct will be discarded. The irregular geometries cannot be easily solved by HFSS mesh calculation; thus, HFSS will refine the unconverged part, and request more memory to solve it. For the failed positions, the Poynting vectors from neighboring areas are used instead, which explains the existence of some abnormal points as marked in red dash circles in figure 3.7.

3.3 Quasi-Optical Setup and Results Using Actual Fingerprints

The theoretical study presented in the previous section demands for experimental verification. Thus, a quasi-optical system is used to perform the experiment of fingerprint

image using THz waves. Its simplified diagram is shown in figure 3.8a and the flow chart is shown in 3.8b. Signal is generated from the vector network analyzer (VNA), upconverted to THz by the VNA extender, and illuminated as a Gaussian beam by the horn antenna. The off-axis parabolic mirror reflects the beam to the hemispherical lens. The hemispherical lens and the silicon extenders focus the beam to a spot on the target. The reflected beam is downconverted to low-frequency and read by VNA.

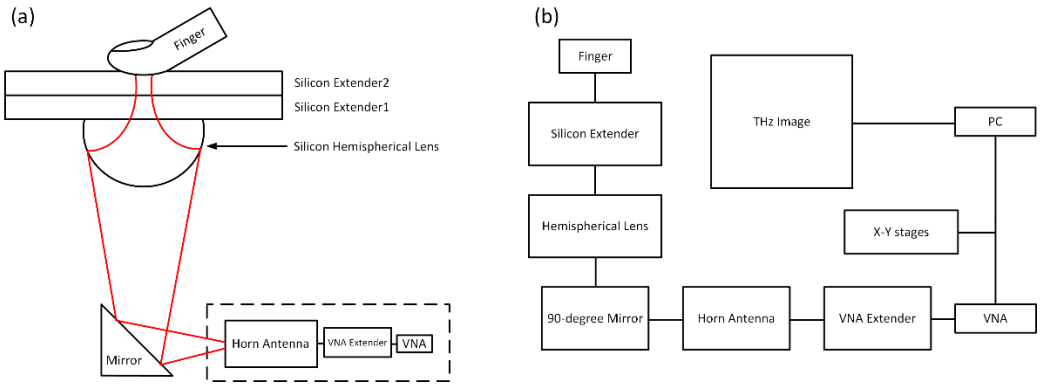

Figure 3.8 (a) The simplified diagram of the Gaussian quasi-optical system: Signal is generated from the vector network analyzer (VNA), upconverted to THz by the VNA extender, and illuminated as a Gaussian beam by the horn antenna. The off-axis parabolic mirror reflects the beam to the hemispherical lens. The hemispherical lens and the silicon extenders focus the beam to a spot on the target. The reflected beam is downconverted to low-frequency and read by VNA (b) Flow chart: LabVIEW is used to control the stages and collect the data from VNA ; MATLAB is used to plot the THz image.

The system is split into two main parts—the signal transceiver and the optics. The signal transceiver includes a VNA, a VNA extender, and a horn antenna. The signal frequency range of the VNA is from 1 GHz to 24 GHz. However, with the VNA extender, the frequency range is multiplied to 325 GHz to 500 GHz. The transceiver schematic diagram is shown in figure 3.9a. The low-frequency wave (RF (radio frequency) signal, 12 GHz) propagates from VNA and multiple to high frequency. Then part of the wave emits from horn antenna. The rest part mixes with the wave (comes from the LO (local

ossicilater) after multipled) as the Ref (reference) signals. The Ref signal corresponds to how much power emit to the antenna. The reflected wave is received by the horn antenna, mixes with the wave (comes from the LO after multipled), downconverted to low frequency as the Meas (measurement), and read by VNA. The S-parameter, for example S_{11}, is Meas devided by Ref. Figure 3.9b shows the VNA extender side view and 3.9b shows the back view.

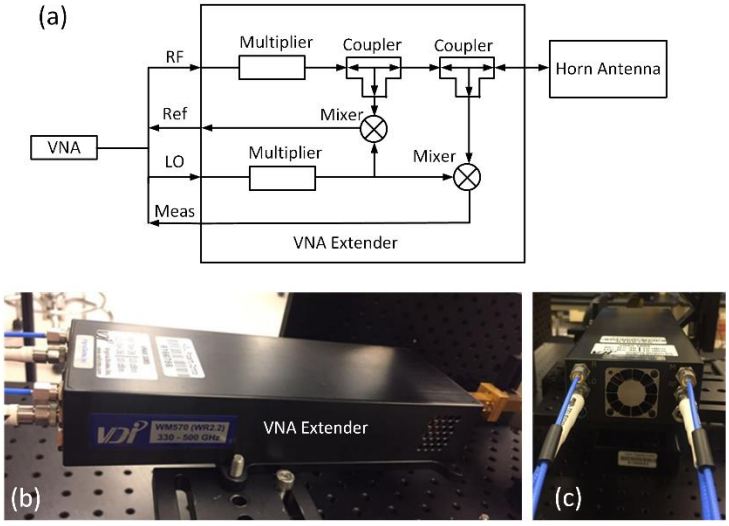

Figure 3.9 (a) The signal transceiver schematic diagram. The transmitted low-frequency waves multiple to high-frequency, mix with LO as Ref; the received high-frequency waves mix with LO, downconvert to low frequency as Meas. (b) VNA extender side view. (c) VNA extender back view.

The optics consist of an off-axis parabolic mirror and a hemispherical lens. The mirror reflects the Gaussian beam to the hemispherical lens. The hemispherical lens focuses the beam to a spot with the help of extenders. Two extra silicon extenders are utilized to extend the distance to achieve the focusing point. Moreover, the hemispherical lens can be glued on the first extender to achieve fixing. The VNA extender, horn antenna, mirror, hemispherical lens and the extender 1 are moveable with linear stages as

shown in figure 3.10a, while the extender 2 is fixed. The system loss is measured to be around 10dB. Figure 3.10bcde show the photograph of the system with different angles.

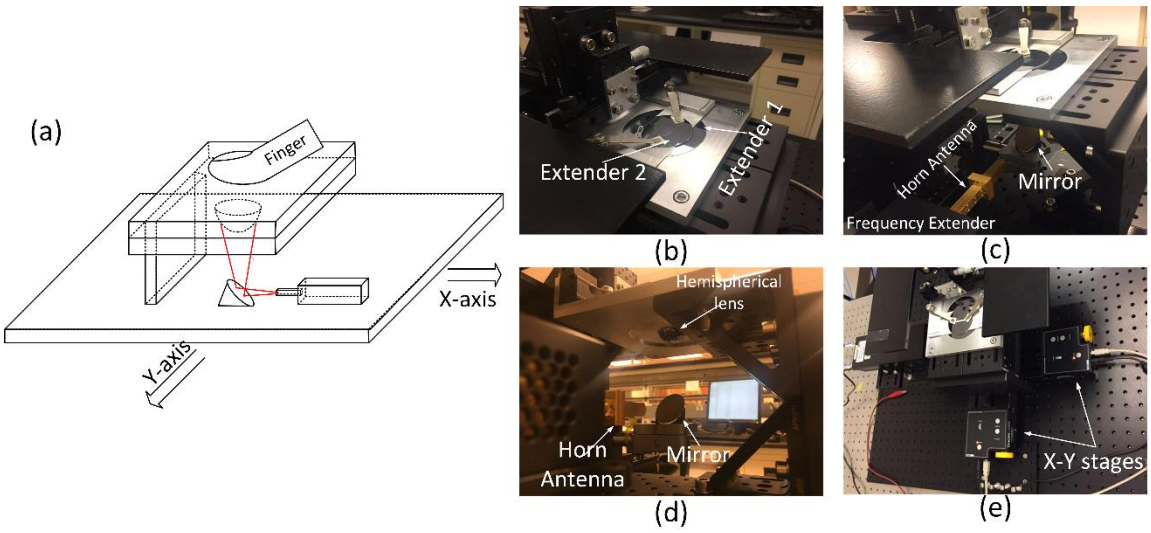

Figure 3.10 (a) The side view of the setup: VNA extender, horn antenna, hemispherical lens, first silicon extender are moveable with X-Y linear stage, except for the second silicon extender, which holds the imaging sample. Gaussian quasi-optical system photograph (Subwavelength THz imaging system): (b) Extender 1 fixes the hemispherical lens, and it is movable with the source part and optics by the stages; extender 2 is holding the device under test, and it is unmovable; (c) The frequency extender boosts the beam frequency to THz, and the beam emits from the horn antenna; (d) The 90-degree mirror reflects the beam to the hemispherical lens, and the lens focuses the beam to a spot; (e) The X-Y linear stages move the transeiver and optics parts to achieve raster scanning.

The imaging with the aforementioned Gaussian quasi-optical setup is still in progress. In the experiment, the source illuminates the electromagnetic wave and optical components focus the wave on a small spot. In the same way, the reflected wave propagates back to the source and the vector network analyzer (VNA) measures the reflected signal power. The ongoing measurement is for an actual human finger, as shown in figure 3.11a. The scanning area is 4 mm by 4 mm with 100 um scanning step. The image scanning process takes 25 minutes. Durning the process, to avoid the finger movements, which can cause the distortion in the image results, a rigid metallic rod is

taped with the index finger as shown in figure 3.11a. In the same way, the other fingers are taped on the stage to finger stabilization. The ridges and valleys are clearly detected, for example on figure 3.11bc, the return loss magnitude is normalized to 0 dB. Thus, the yellow lines are ridges and blue lines represent valleys. Although the acquired images feature high spatial resolution, identifying the sweat duct locations is not straightforward. The strong reflection between the silicon substrate (ε_r= 12) and the skin (ε_r= 4) in conjunction with the fine ripples across the skin ridges, mask the THz wave interaction with the sweat ducts. Further investigation in needed to decouple the two signals and retrieve the sweat duct pattern images.

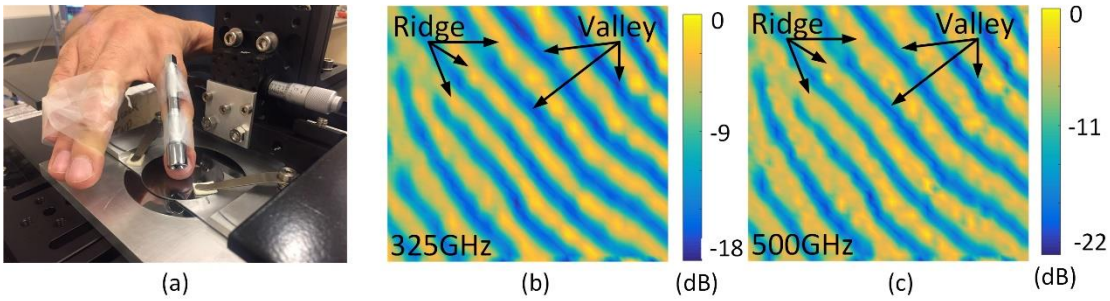

Figure 3.11 (a) The THz image experiment for an actual human finger. The index finger is taped with a rod to achieve fixing. (b)The THz image at 325 GHz and (c) 500 GHz. Ridges, valleys, and sweat ducts are clearly detected. The magnitude is normalized to 0dB.

CHAPTER 4

FINGERPRINT SCANNING USING NEAR-FIELD DETECTION

The results of Chapter 3 show that the tissue with different geometries and physical properties (e.g., dielectric constant and conductivity) reflect different power. However, the Gaussian quasi-optical setup has to scan the finger point by point, which is time-consuming to be applied in practice. Additionally, such approach requires bulky and heavy focusing components (e.g. mirrors and lenses) that are impractical for applications where size and weight are crucial. A terahertz array antenna, shown in figure 4.1a, is an attractive solution for this issue. The terahertz array is comprised by multiple small terahertz antennas. Each terahertz antenna has a feeding line and all the feeding lines make up the feeding network. By controlling the signals through the feeding network, all terahertz array antennas can emit the terahertz wave at once and receive the reflected signal, which significantly accelerates the fingerprint scanning process and reduces the imaging system's size dramatically. To study this design's imaging performance, a single antenna is horizontally scanned , as depicted in figure 4.1b. The numerical study of different types of antennas is performed using a full-wave electromagnetic solver, and the experimental results are collected from the fabricated antennas.

Figure 4.2ab shows the phantom model for simulation in HFSS. It consists of two parts: top undulation and sweat ducts. The grey rectangle with ridges and valleys is the top undulation, which represents the epidermal layer undulation. The bottom undulation, which is the dermal layer undulation, is ignored in the simulation for minimizing the

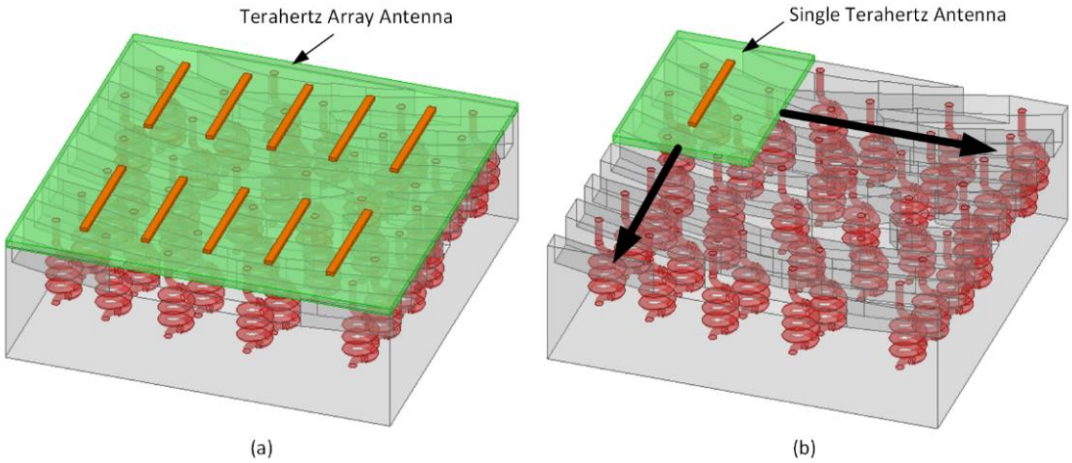

Figure 4.1 (a) THz imaging approach by using THz array antenna with a 3D phantom fingerprint model. (b) One Terahertz antenna with horizontally scanning is used to replace the array antenna.

computation time. The red helical structures, which are inside the epidermal layer and always located along the ridges, represent the sweat ducts. The top undulation and the sweat ducts are designed in SolidWork 2016 and are captured from an actual fingerprint. Since the real fingerprint size is too small to be fabricated, for example, the diameter of the sweat duct pipe is around 50um, the phantom model is enlarged by 20 times from the actual size.

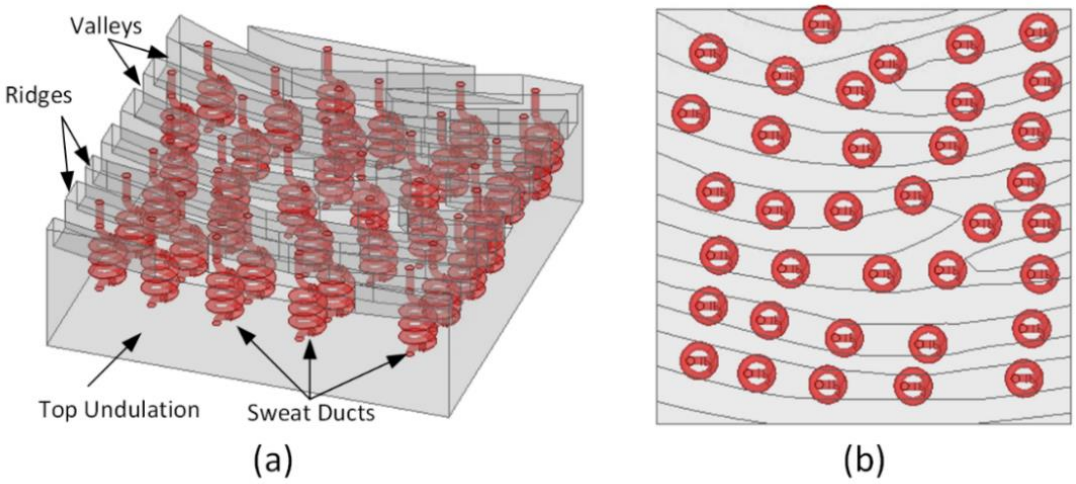

Figure 4.2 HFSS 20-time enlarged phantom model 3D side view (a) and top view (b). The undulation represents the epidermal layer undulation. The Red helical ducts represent sweat ducts.

4.1 Antenna Field Regions

The space surrounding an antenna can be split into three regions: reactive near-field region, radiating near-field (Fresnel) region, and the far-field (Fraunhofer) region as shown in figure 4.3 (Balanis, 2016).

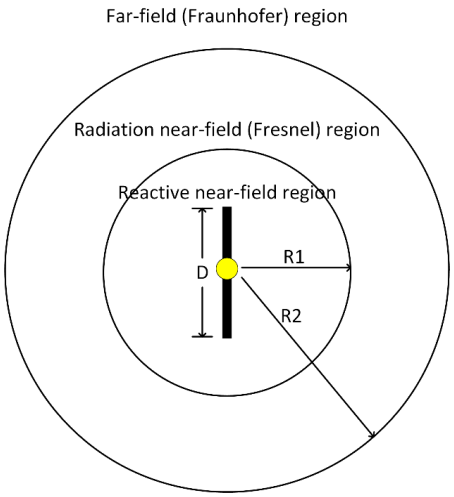

Figure 4.3 Field region of an antenna.

The reactive near-field region, which is predominated by the reactive field immediately surrounds the antenna. For most of the antennas, the reactive near-field boundary R_1 is,

$$R_1 = 0.62\sqrt{D^3/\lambda} \quad (4.1)$$

where D is the largest dimension of the antenna and λ is the wavelength in the surrounding medium. Near-field radiation is the region between the reactive near-field and the far-field where the radiation field predominates. The inner boundary of radiation near-field region is R_1 and the outer boundary R_2 is,

$$R_2 = 2\,D^2/\lambda \quad (4.2)$$

Far-field is the region where the field distribution is independent of the distance from the antenna. As in the near-field region, the far-field region is also referred to

Fraunhofer region based on optical terminology. Our design operates at 20GHz, where the wavelength is 15mm. The distance from the antenna to the sample is less than 0.5mm. Thus, it can be classified to the reactive near-field region.

4.2 Coaxial Probe

A coaxial probe is shown in figure 4.4a. In the near-field, the coaxial probe can be approximately treated as a monopole antenna. The coaxial probe has a strong energy focusing ability in near-field, since the metal pin is fabricated in a very small dimension compared to the target.

Figure 4.4 A coaxial probe.

4.2.1 Numerical Validation Skin Images Using a Scaled Skin Model

Figure 4.5a shows the 20-time scaled phantom model with a coaxial probe in HFSS. It consists of a copper pin in the center, a Teflon cylinder around the pin, and a wave port on the top as shown in figure 4.5b. The electric field distribution on a surface, which is placed 0.5 mm below the pin, is plotted in figure 4.5cde. The E-z component is much stronger than the E-x and E-y components. The coaxial probe is horizontally shifted upon the model to achieve the scanning process. The image is acquired by computing the return loss (S_{11}) data at each position.

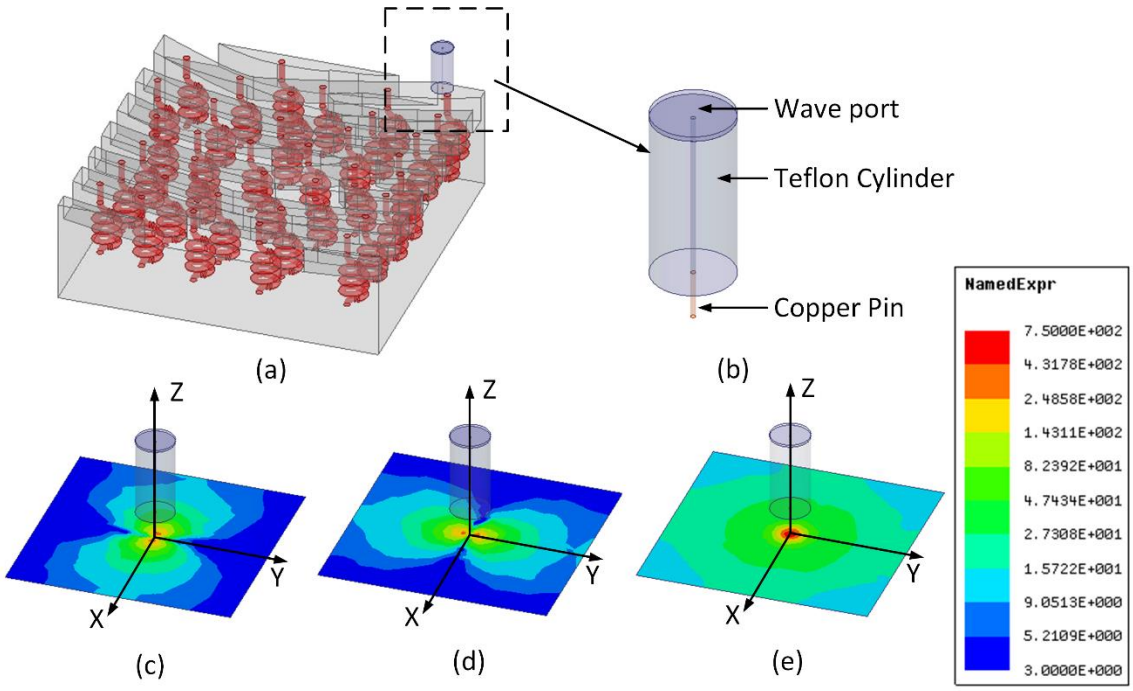

Figure 4.5 (a) The phantom model with a coaxial probe. (b) The coaxial probe. (c) The E-x component magnitude plot of a surface which 0.5mm under the metal pin. (d) The E-y component magnitude. (e) The E-z component magnitude. The E-z component dominates in the field distribution. The field distribution figures are used in the same dB scale.

Since the full-wave simulation is time-consuming, only the quarter part (as shown in the black square in figure 4.6a) was simulated. The image results without sweat ducts are shown in figure 4.6b (10 GHz), 4.6c (15GHz), and 4.6c (20GHz). Since the model is enlarged by 20 times, the frequency should be multiplied by 20 as well, corresponding to 200 GHz, 300 GHz, and 400 GHz, respectively. Ridges and valleys are clearly detected. The yellow lines represent valleys, and the blue lines represent ridges. The images with sweat ducts are shown in figure 4.7bcd. Both ridges, valleys and sweat ducts can be identified. The deep blue spots are the sweat ducts, as depicted in figure 4.7b. By increasing the frequency, the blue spot changes its shape. Specifically, as the frequency increases, the sweat duct images (blue spots) expand to its neighbor part as shown in figure 4.7bcd. To investigate this phenomenon, two more groups of simulations are

performed, using sweat ducts with different water levels. Because the water level inside the sweat duct represents the perspiration level, and may effect the intensity of the reflected power.

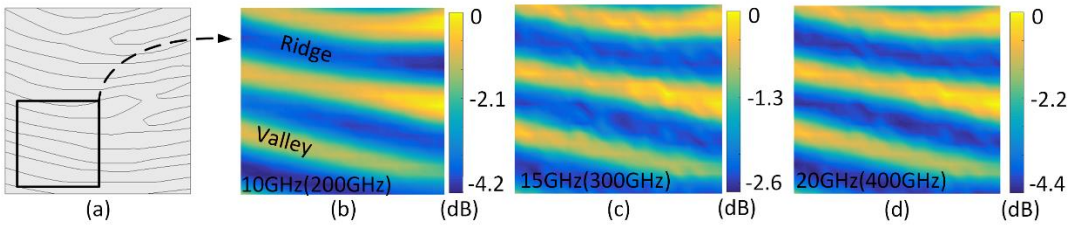

Figure 4.6 (a) Simulation area and HFSS images without sweat ducts using the coaxial probe at (b) 10 GHz, (c) 15 GHz, and (d) 20 GHz. The frequency should be multiplied by 20, corresponding to 200 GHz, 300 GHz, and 400 GHz, due to the 20-time scaled model. The magnitude for all the figures is normalized to 0 dB.

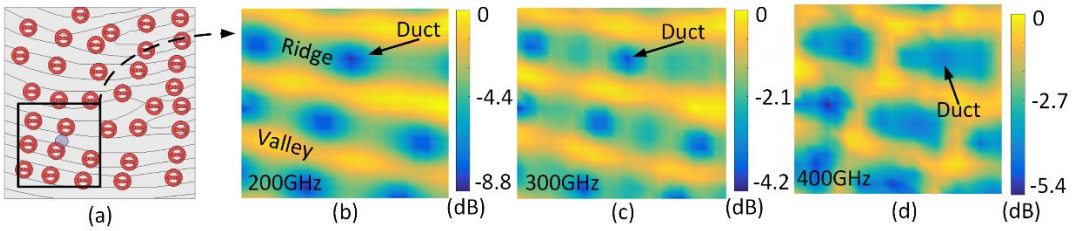

Figure 4.7 (a)Simulation area and (b) HFSS image results with sweat ducts using the coaxial probe at 10 GHz, (c) 15 GHz and (d) 20 GHz. The dash square box changes color from light blue to dark blue with frequency. This phenomenon may be caused by the structure of the sweat ducts.

The sweat duct structure can be split into a vertical pipe and a helical pipe as shown in figure 4.8a. The previous images are generated when both vertical pipe and helical pipe are filled with water. In the second case, only the helical duct is filled with water while the vertical pipe remains empty, as shown in figure 4.8b.

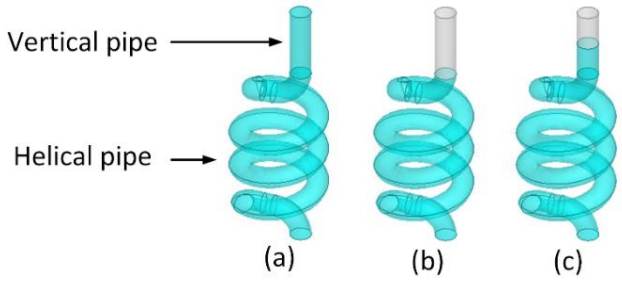

Figure 4.8 (a) Water filled in the duct and the pipe. (b) Water only filled in the duct. (c) Water filled in duct and half pipe.

The simulation results for the second case are shown in figure 4.9bcd. As shown in figure 4.9b, there is no evidence of sweat ducts when the frequency is 10 GHz, only ridges and valleys can be detected, while the sweat ducts are presented in figure 4.7b. When the frequency is increased to 20 GHz, the sweat ducts images slightly show up, as shown in figure 4.9d. In the third case, the helical pipe is filled with water and the vertical pipe is half-filled with water. The simulation results for the third case are shown in figure 4.10bcd. The intensity of the sweat ducts images in figure 4.10 is in between the figure 4.7 and figure 4.9 as we expected.

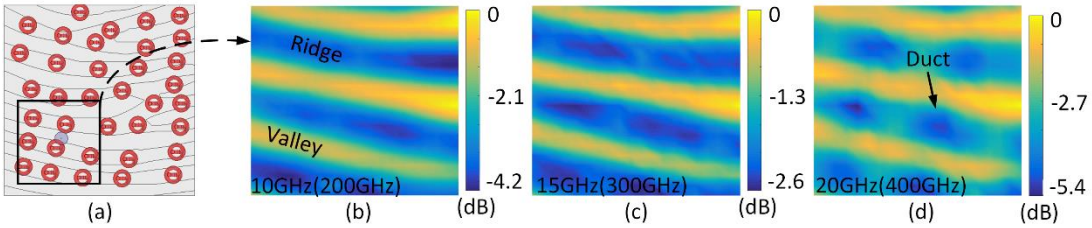

Figure 4.9 (a) HFSS simulation model and the image results with vertical vacuum pipe at (b) 10 GHz, (c) 15 GHz, and (d) 20 GHz. Only the 20GHz image shows the sweat ducts.

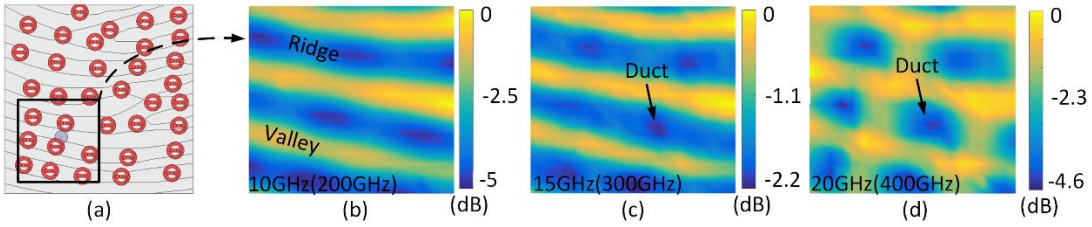

Figure 4.10 (a) HFSS simulation model and the image results with vertical half vacuum pipe at (b) 10 GHz, (c) 15 GHz, and (d) 20 GHz. Only the 20GHz image indicates the sweat ducts.

The simulation results indicate that the water in the vertical pipe strongly affects the resulting images. This result can be explained from two aspects. Firstly, the coaxial probe has vertical polarization, and the vertical pipe has a strong polarization in the z-axis (as shown in 4.5e), while the helical pipe has the circular polarization, which leads to a better coupling between the vertical pipe and the coaxial probe. Secondly, the helical structure has a resonant frequency around 20 GHz (after 20-time scaled). These two reasons indicate that for better imaging quality, an antenna with planar polarization has a better coupling with the sweat ducts.

4.2.2 Experimental Measured Skin Images Using a 3D Printed Scaled Phantom

For the experimental measurement, we decided to fabricated the phantom. The 20-time enlarged fingerprint phantom, which used in the measurement, has two undulations as shown in figure 4.11a—the top undulation represents the epidermal undulation, and the bottom undulation represents the dermal undulation (in the previous simulations, only the top undulation is used to accelerate the simulations). These undulations are different in terms of geometry. In figure 4.11a, the small holes on the top undulation are represented as pores. The holes are connected with the helical pipes as shown in the 4.12, which could be treated as sweat ducts. The helical pipes are connected to a rectangular chamber (figure 4.11b) as shown in figure 4.12, which is placed underneath the bottom ridges. The rectangular chamber represents the dermal layer and is used to store the water representing sweat. By combining the undulation and base, the

final fingerprint model is established as shown in figure 4.11(c). The length and width of the model are both 50 mm, while the height is 26 mm.

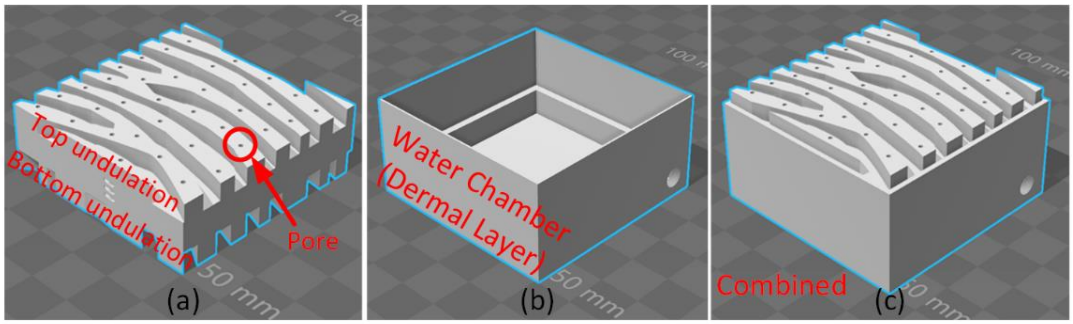

Figure 4.11 (a) Top undulation and bottom undulation with sweat ducts in between. (b) The rectangular water chamber represents the dermal layer and stores the water. (c) The final model.

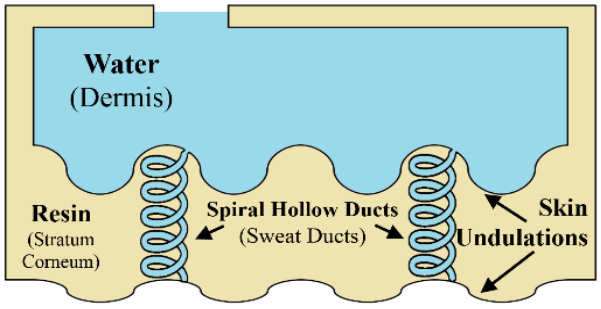

Figure 4.12 The fingerprint model cross-section simplified diagram.

The proposed model was fabricated at Chandler Techshop, Arizona. Figure 4.13ab shows the top view and the side view of the fabricated model. The model is made of polymer resin from Formlabs, and its dielectric constant is around 3. Due to the roughness of the bottom surface caused by the 3D printing technology, polishing was conducted by ASU machine shop. The measurement splits into two groups—1) with water in the chamber and 2) without water in the chamber. A syringe is used to inject the water into the chamber as shown in figure 4.13c.

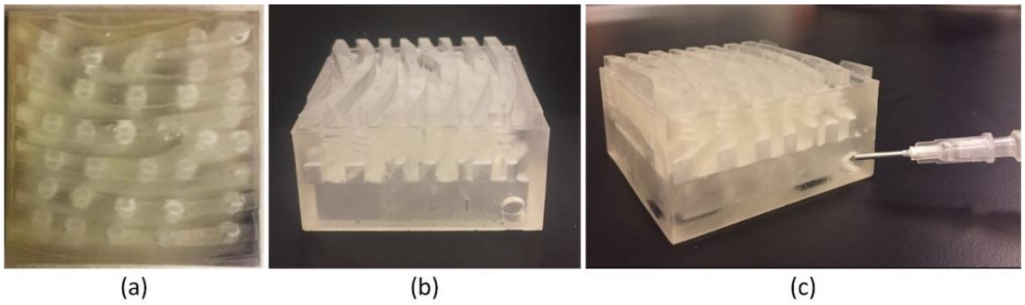

Figure 4.13 The top view (a) and the side view (b) of the 20-time enlarged fingerprint model. (c) A syringe is used for water injection.

Figure 4.14a shows the near-field detection setup with a coaxial probe. The coaxial probe could be treated as a near-field monopole antenna, and it is connected to the VNA. The X-Y linear stages are used to move the position of the model to result the whole image. Both the VNA and the stages are connected to the laptop and controlled by LabVIEW as shown in figure 4.14b. During the scanning, the model is taped on the stages. The coaxial probe is fixed as close as possible to the model (less than 1mm as shown in figure 4.15).

Figure 4.16a shows the top view of the model and figure 4.16bcd are the images from the measurement (without water) at 10GHz, 15GHz, and 20GHz respectively. The Ridges and valleys can be clearly identified from the image at 10 GHz as shown in figure4.16b. The yellow lines are valleys, and the blue lines are ridges, which is in

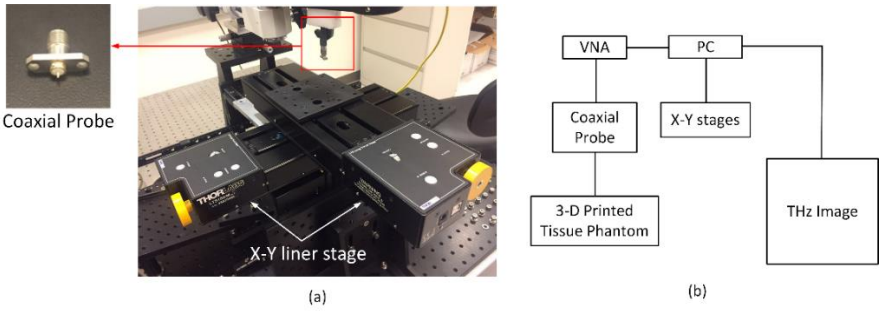

Figure 4.14 Near-field detection setup with a coaxial probe in the Lab (a) and the flow chart (b).

agreement with the numerical results. However, when the frequency is increased to 15 GHz, some blue spots show up and distortion occurs, as shown in figure 4.16c. At 20 GHz, it becomes difficult to recognize the ridges and valleys. The most important reason is that at high frequencies, the wavelength becomes smaller. Thus, multiple reflections inside the model will distort the image.

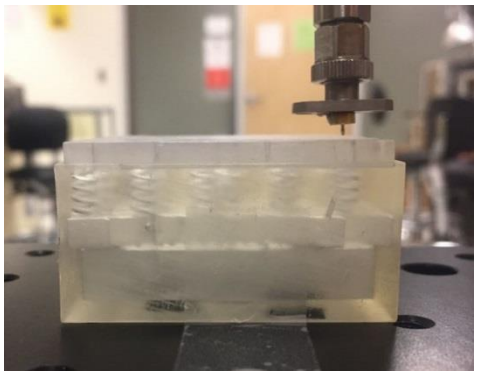

Figure 4.15 The measurement side view. The distance from the coaxial probe to the model is less than 0.5mm.

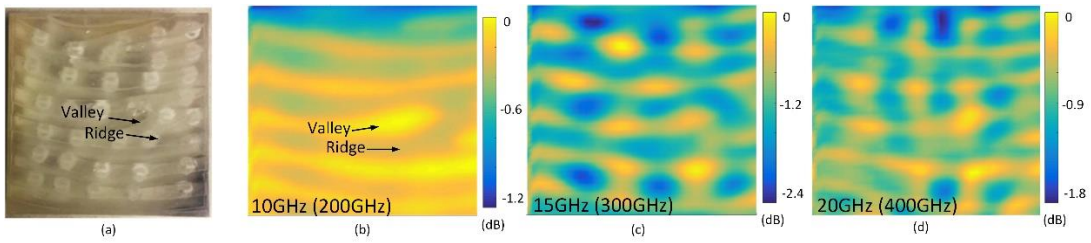

Figure 4.16 (a) The 20-time scaled phantom and coaxial probe measurement image results without water on (b) 10 GHz, (c) 15 GHz, and (d) 20 GHz. On 10 GHz, ridges and valleys are clearly detected, however, images distort at 15 GHz and 20 GHz. This is due to the multiple reflections inside vacuum model at the higher frequency.

Then the measurement with the existence of water is conducted. The water is injected from the side hole and the chamber and sweat duct volume is filled with water. The images from the measurement at 10GHz, 15GHz and 20GHz are shown in figure 4.17. In addition to the ridges and valleys, the sweat ducts can be detected at 10 GHz and

15 GHz as marked by the dashed red line. However, the distortion still occurs when the frequency is increased to 20 GHz. By comparing the image at 10 GHz with the one at 15 GHz, it can be stated that the position of the sweat ducts (blue spots) changed, which matches with the phenomenon from HFSS simulation. Another important phenomenon is the influence of the water. The images in figure 4.17 are more clear than the images in figure 4.16. The results verify that the water is more lossy than the air, in other words, the water absorbs more energy than air. Even through the distance between the probe and the model is controlled to be less than 0.5mm, this distance varies from different measurements. Thus, the measurement is unrepeatable.

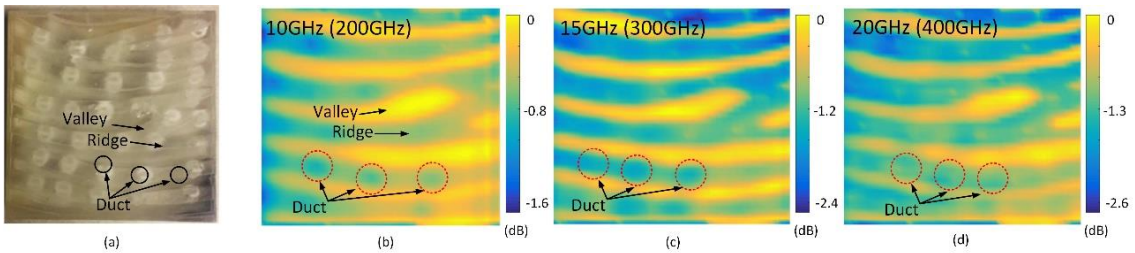

Figure 4.17 (a) The 20-time scaled phantom and coaxial probe measurement image results with water on (b) 10 GHz, (c) 15 GHz, and (d) 20 GHz. Both ridges, valleys, and sweat ducts are detected. Water enhanced the images quality which indicated that water is more loss than air.

The results above suggest that with the utilization of the coaxial probe, clear images can be recorded. However, because this type of antenna has a rod body, the coaxial probe is hard to be integrated. Also, the feeding network for a “coaxial probe” array is challenging. Moreover, the coaxial probe does not have the circular polarization which leads to a weak coupling with the sweat ducts. To deal with those issues, other types of antennas are investigated in the next section.

4.3 Slot-Dipole Antenna

This section investigates a slot dipole antenna which is fabricated on a printed circuit board (PCB). Due to its plane body, the slot antenna is much easier to be integrated into an array than the coaxial probe. A slot antenna consists of a flat metal surface (as the ground plane) with one or more slots cut out. When the surface is driven as an antenna, the slot radiates electromagnetic waves through the edge of the slot. In our case, the slot antenna can radiate the wave through the edge and the wave propagates into the substrate as shown in figure 4.18a. The substrate's dielectric constant is as close as the epidermal layer (3.8) to avoid the reflection between the interface. Figure 4.18b presents a close look of the slot dipole antenna with a lumped port in the center. The width of the antenna is set to be 0.4 mm and the length is set to be 8 mm to achieve a resonant frequency of 15 GHz. As shown in figure 4.18c, the input impedance z_{in} of the antenna is 296.71+j78.06 at 15 GHz.

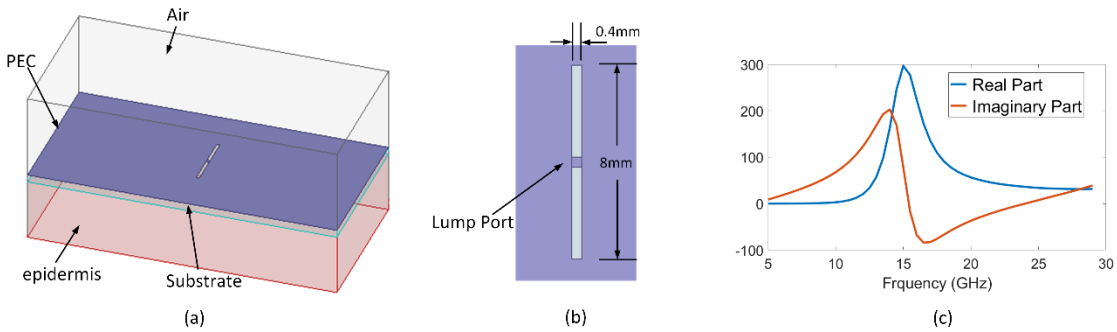

Figure 4.18 (a) A slot dipole antenna model. (b) The length is 8 mm and width is 0.4 mm. (c) The input impedance is 296.71+j78.06 on 15GHz.

The lumped port in the antenna center is used to avoid the influence of feeding network to focus on the slot-dipole performance. When the size of the slot-dipole is decided, a wave port with a long feeding line is used to replace the lump port as shown in

figure 4.20a. The wave port is used to imitate the SMA connector and it will be replaced by the SMA connector in the fabrication. Since the impedance of SMA connector is 50 Ohms, the impedance of the wave port and the feeding line needs to be set to 50 Ohms for matching purpose.

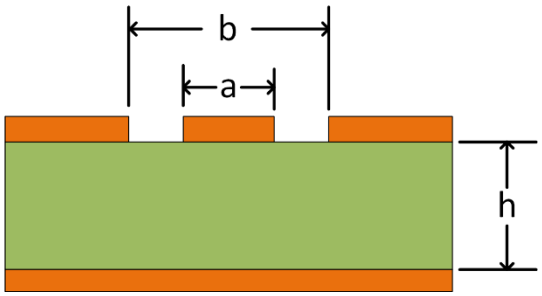

Figure 4.19 Cross-section view of a grounded Coplanar Waveguide(CPW) line.

The original formulas for the grounded Coplanar Waveguide (CPW) line geometry calculation are in (Wadell, 2003). The formulas use "a" for the track width and "b" for the sum of the track width plus the gaps as shown in 4.19. The characteristic impedance of the grounded CPW line is

$$Z_0 = \frac{60\times\pi}{\sqrt{\varepsilon_{eff}}} \times \frac{1}{\frac{K(k)}{K(k')} + \frac{K(kl)}{K(kl')}} \quad (4.3)$$

where $K(k)$ is the first kind of the Elliptical Integrals,

$$k = \frac{a}{b} \quad (4.4)$$

$$k' = \sqrt{1-k^2} \quad (4.5)$$

$$kl' = \sqrt{1-kl^2} \quad (4.6)$$

$$kl = \frac{tanh\left(\frac{\pi\times a}{4\times h}\right)}{tanh\left(\frac{\pi\times b}{4\times h}\right)} \quad (4.7)$$

$$\varepsilon_{eff} = \frac{1 + \varepsilon_r \times \frac{K(k')}{K(k)} \times \frac{K(k)}{K(k')}}{1 + \frac{K(k')}{K(k)} \times \frac{K(k)}{K(k')}} \quad (4.7)$$

where ε_r is the dielectric constant of the substrate (3.8 in our simulation). By setting the width of the gap to 0.1mm, the track to 1mm, and the thickness h to 1000mm (infinity), the ε_{eff} can be calculated with the result to be 2.4 and the characteristic impedance is 50 Ohms. The 50 Ohms feeding line is shown in figure 4.20a and the simulated return loss is shown in figure 4.21 black line. Since the antenna is directly connected to the feeding line, the mismatch will influence the return loss performance. Thus, a five-step binomial impedance transformer is needed to match the antenna to the feeding line and enhance the performance. After calculation, the impedance of the line L1 is 125 Ohms, L2 is 118 Ohms, L3 is 94 Ohms, L4 is 66.5 Ohms, and L5 is 53 Ohms as shown in figure 4.20b. The width of the lines can be calculated in the same way as the calculation for the 50 Ohms feeding line. However, according to the minimum milling width (0.2mm) of the milling machine, the width of the lines in the model needs to be adjusted. The return loss (figure 4.21 red line) after the binomial impedance transformer shows that the slot dipole antenna has two sharp points at 14GHz and 15.5GHz. The electrical field distribution of a surface, which is 0.5mm to the antenna, is plotted in figure 4.22. By comparing to the coaxial probe, the E-y component is stronger for the slot-dipole antenna.

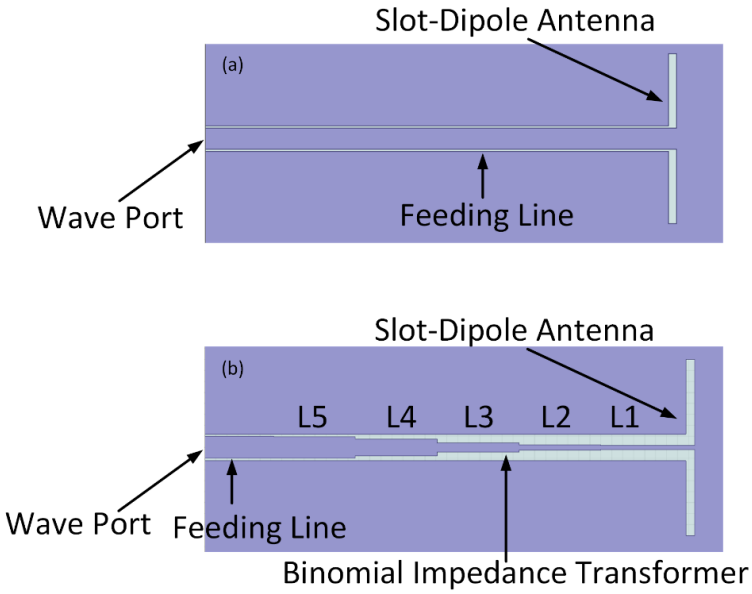

Figure 4.20 (a) 50 Ohms feeding line and a wave port are used to replace the lump port. (b) A five-step binomial impedance transformer is used to match the impedance from the antenna to the wave port.

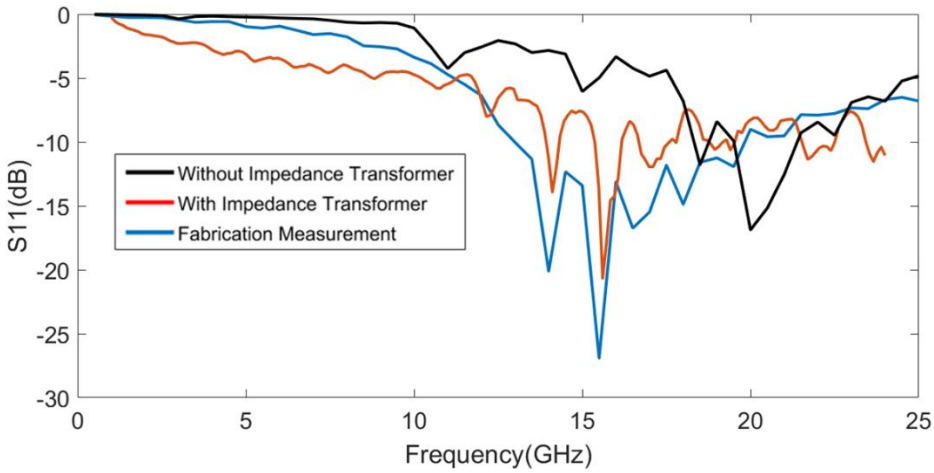

Figure 4.21 The return loss for simulation without impedance transformer, with impedance transformer, and measured after fabrication. The simulation result matched with the measurement result.

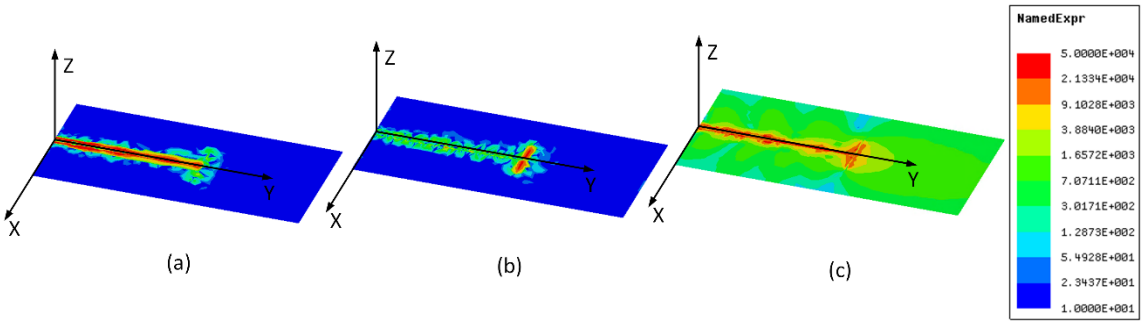

Figure 4.22 (a) The E-x component magnitude plot of a surface which 0.5mm under the slot-dipole antenna. (b) The E-y component magnitude. (c) The E-z component magnitude. The E-y component is stronger in E-total when compared to the coaxial probe in the previous section.

Due to the electrically large antenna, the numerical simulation becomes infeasible and only the experimental results are shown. The board used in the fabrication is RO4003Pro from Rogers company. Its dielectric constant is 3.66 and the thickness of the board is 1mm with metalization on the both sides. The fabrication is done by a milling machine as shown in figure 4.23a. The SMA connector and the fabricated antenna are shown in figure 4.23bc. The return loss of the antenna is shown in figure 4.21 with a blue line. By comparing the return loss of the fabricated slot antenna and simulated slot

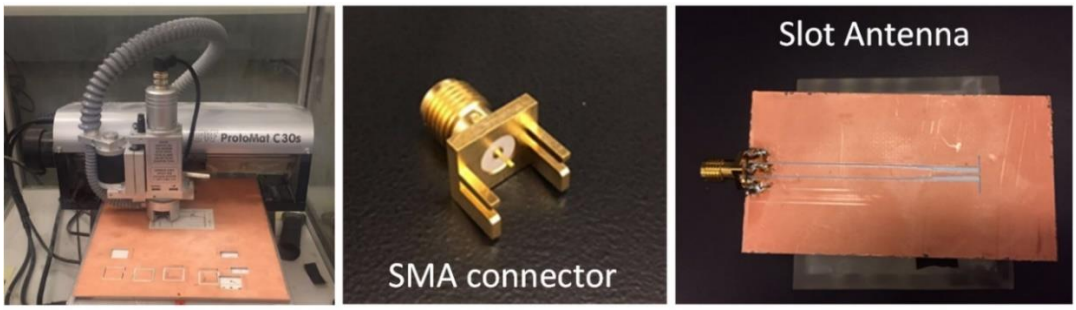

Figure 4.23 (a) The ProtoMat C30s milling machine. (b) The SMA connector. (c) The fabricated slot-dipole antenna.

antenna shown in figure 4.21, the results are reasonably matched. The small difference in S11 magnitude could be explained by the resolution limit of the milling machine.

The measurement with the fabricated slot-dipole antenna (with water in the chamber) is accomplished and the results are shown in figure 4.22. The ridges and valleys do not show up in the image at 10 GHz, but at 15 GHz and 20 GHz, the ridges and valleys start to appear. However, the images are partially distorted at all frequencies which can be explained by the fact that the slot dipole antenna does not have a good beam focusing ability. In other words, the width of the slot feed line and the impedance transformer is too large compared to the width of the slot dipole antenna as shown in figure 4.22 and 4.23c. These slots may behave as part of the antenna during the measuring and effect the slot-dipole antenna performance.

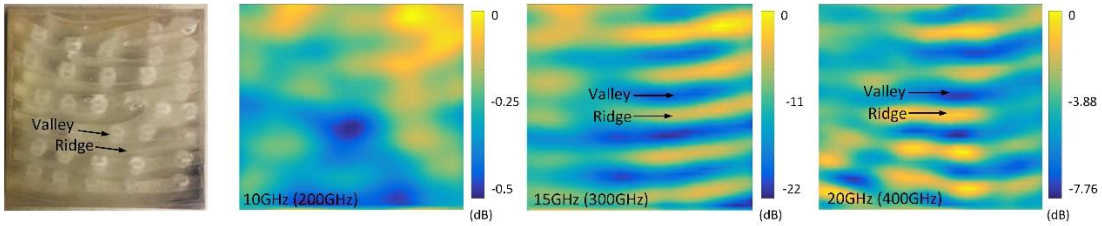

Figure 4.24 (a) The 20-time scaled phantom and slot-dipole antenna measurement image results with water on (b) 10 GHz, (c) 15 GHz, and (d) 20 GHz. The image results are partially distorted since the width of the slot feed line and the impedance transformer is too large compared to the width of the slot-dipole antenna, making them radiate and behaving as part of the antenna.

CHAPTER 5

CONCLUSIONS

In this work, a new fingerprint imaging method for the next generation fingerprint biometrics identification was presented. The most important part of the method is to detect the sweat duct image and combine it with ridges and valleys. Due to the THz waves have the ability to penetrate fingerprint surface and the sweat duct has a helical pipe structure which leads to a resonant frequency around 490 GHz, the operating frequency is around 200 GHz to 500 GHz.

Two imaging approaches were presented: Gaussian quasi-optical system and near-field detection with THz antennas. The numerical validation for the Gaussian quasi-optical system was simulated in HFSS software. The image results clearly capture the ridges, valleys, and sweat ducts information. The best result is a 4 mm by 4mm image from a human finger, where ridges and valleys are clearly detected. The focused imaging approach provides exceptional image spatial resolution (<80 μm), however, it failed to reproduce the sweat duct pattern. The strong wave reflection on the silicon substrate-tissue interface masked the weaker sweat duct – terahertz wave interaction. A possible future investigation will attempt to detect sweat ducts by measuring the inherent dichroism effect due to the helical structure.

Additionally, the analysis of near-field imaging investigated using two different antenna geometries. As such, we designed and tested a coaxial probe and a slot dipole antenna. To evaluate the imaging performance, we manufactured a 20-time scaled finger skin phantom using 3D fabrication techniques. The coaxial probe showed excellent image spatial resolution due to the small footprint that result in highly concentrated field

distribution on the phantom skin. Also, the probe showed a reasonable interaction with the sweat ducts as was expected from the numerical analysis. On the other hand, the slot antenna, although more efficient in terms of return loss, resulted in limited spatial resolution images and failed to identify the sweat ducts. The large antenna footprint results in a significantly bigger field spot that results in compromised imaging performance. For all the raster scanning imaging experiments, we used highly precise (<2μm) translation stages that were computer controlled by LabVIEW. The necessary LabVIEW coded was implemented to achieve an automated and accurate data acquisition from the Vector Network Analyzer (VNA) while appropriately synchronizing the x-y translation stage.

REFERENCES

About Touch ID security on iPhone and iPad - Apple Support. (2015, Nov. 3). Retrieved from https://support.apple.com/en-us/HT204587

Aditya Tiwari, 2016 March 27. How Does a Fingerprint Scanner Work — The Application of Biometrics. Fossbytes. Retrieved from https://fossbytes.com/how-does-a-fingerprint-scanner-work-the-application-of-biometrics/

ANSYS HFSS: High Frequency Electromagnetic Field Simulation. Retrieved from http://www.ansys.com/products/electronics/ansys-hfss

Ashbaugh, D. R. (1999). *Quantitative-qualitative friction ridge analysis: An introduction to basic and advanced ridgeology*.

Balanis, C. A. (2016). Antenna theory: Analysis and design.

BBC - A History of the World - Object : ROMAN FLOOR TILE WITH HAND PRINT. (2003). Retrieved from http://www.bbc.co.uk/ahistoryoftheworld/objects/alkGH4JcQfGjGL61edjRCw

B. E. A. Saleh, M. C. Teich, 2007. Fundamentals of Photonics 2nd. Hoboken, New Jersey: John Wiley & Sons.

Bryan E., Ruth M., David A., Donald D., Michael P. (2001). THz Imaging and Spectroscopy of Human Skin in-vivo. Terahertz imaging and spectroscopy of human skin in vivo. Proc. SPIE 4276, 1-10.

Cooper, K. B., Dengler, R. J., Llombart, N., Thomas, B., Chattopadhyay, G., & Siegel, P. H. (2011). THz Imaging Radar for Standoff Personnel Screening. IEEE Transactions on Terahertz Science and Technology, 1(1), 169-182.

Derakhshani, R., Schuckers, S. A., Hornak, L. A., & O'Gorman, L. (2003). Determination of vitality from a non-invasive biomedical measurement for use in fingerprint scanners. Pattern Recognition, 36(2), 383-396.

Ferguson, B., Wang, S., Gray, D., Abbot, D., & Zhang, X. (2002). T-ray computed tomography. Optics Letters, 27(15), 1312.

Fitzgerald, A. J., Wallace, V. P., Jimenez-Linan, M., Bobrow, L., Pye, R. J., Purushotham, A. D., & Arnone, D. D. (2006). Terahertz Pulsed Imaging of Human Breast Tumors. Radiology, 239(2), 533-540.

Galbally, J., Alonso-Fernandez, F., Fierrez, J., & Ortega-Garcia, J. (2012). A high-performance fingerprint liveness detection method based on quality related features. Future Generation Computer Systems, 28(1), 311-321.

Galton, F. (2015). *Finger prints*.

Goldsmith, P. F. (1998). Quasioptical systems: Gaussian beam quasioptical propagation and applications.

Hayut, I., Puzenko, A., Ben Ishai, P., Polsman, A., Agranat, A. J., & Feldman, Y. (2013). The Helical Structure of Sweat Ducts: Their Influence on the Electromagnetic Reflection Spectrum of the Skin. IEEE Transactions on Terahertz Science and Technology, 3(2), 207-215.

Grew, N. (1684). The Description and Use of the Pores in the Skin of the Hands and Feet, by the Learned and Ingenious Nehemiah Grew, M. D. Fellow of the College of Physicians and of the Royal Society. *Philosophical Transactions of the Royal Society of London*, *14*(155-166), 566-567.

Hu, B. B., & Nuss, M. C. (1995). Imaging with terahertz waves. Optics Letters, 20(16), 1716.

Hu, Q. (2008). Terahertz quantum cascade lasers and video-rate THz imaging. 2008 International Workshop "THz Radiation: Basic Research and Applications".

Jia, J., & Cai, L. (2007). Fake Finger Detection Based on Time-Series Fingerprint Image Analysis. Lecture Notes in Computer Science, 1140-1150.

Karpowicz, N., Zhong, H., Zhang, C., Lin, K., Hwang, J., Xu, J., & Zhang, X. (2005). Compact continuous-wave subterahertz system for inspection applications. Applied Physics Letters, 86(5), 054105.

Li, S. Z., & Jain, A. K. (2009). *Encyclopedia of biometrics*.

Library - The History of Fingerprinting. (1998). Retrieved from http://www.di-srv.unisa.it/~ads/corso-security/www/CORSO-9900/biometria/Fingerprinting.htm

Matsumoto, T., Matsumoto, H., Yamada, K., & Hoshino, S. (2002). . Optical Security and Counterfeit Deterrence Techniques IV.

Meyer, H. (1998). Six biometric devices point the finger at security. Computers & Security, 17(5), 410-411.

MYTH OF FINGERPRINTS | spectre footnotes. (2009). Retrieved from https://spectregroup.wordpress.com/2009/04/10/myth-of-fingerprints/

National Institute of Justice (U.S.). (2011). The fingerprint sourcebook. Washington, DC: U.S. Dept. of Justice, Office of Justice Programs, National Institute of Justice.

Nearly 85% of schools use tech to take attendance, Education News & Top Stories - The Straits Times. (2017). Retrieved from http://www.straitstimes.com/singapore/education/nearly-85-of-schools-use-tech-to-take-attendance

Palka, N., Panowicz, R., Ospald, F., & Beigang, R. (2015). 3D Non-destructive Imaging of Punctures in Polyethylene Composite Armor by THz Time Domain Spectroscopy. *Journal of Infrared, Millimeter, and Terahertz Waves*, *36*(8), 770-788.

Prints of hands and fingers made by Herschel. Retrieved from http://www.sloughhistoryonline.org.uk/ixbin/hixclient.exe?a=query&p=slough&f=generic_largerimage.htm&_IXFIRST_=1&_IXMAXHITS_=1&t=sl-sl-fatherclemente&%3Dcms_con_core_identifier=sl-sl-1526_herschelfprint-i-01-000.tif&s=CSCPfhW25yo

Putte, T., & Keuning, J. (2000). Biometrical Fingerprint Recognition: Don't get your Fingers Burned. Smart Card Research and Advanced Applications, 289-303.

Robert Triggs, 2016 Dec. 13. How fingerprint scanners work: optical, capacitive, and ultrasonic variants explained. Android Authority. Retrieved from http://www.androidauthority.com/how-fingerprint-scanners-work-670934/

Saleh, B. E., & Teich, M. C. (2013). Fundamentals of photonics.

Tang, H., Lu, Y., Assaderagh, F., Daneman, M., Jiang, X., Lim, M., … Boser, B. E. (2016). 11.2 3D ultrasonic fingerprint sensor-on-a-chip. 2016 IEEE International Solid-State Circuits Conference (ISSCC).

Terahertz radiation - Wikipedia. (2017, May 29). Retrieved, from https://en.wikipedia.org/wiki/Terahertz_radiation

Tewari, P., Kealey, C. P., Bennett, D. B., Bajwa, N., Barnett, K. S., Singh, R. S., … Taylor, Z. D. (2012). In vivo terahertz imaging of rat skin burns. Journal of Biomedical Optics, 17(4), 040503.

The History of Fingerprints. (2017). Retrieved from http://onin.com/fp/fphistory.html

Trichopoulos, G., Mumcu, G., Sertel, K., Mosbacker, H. L., & Smith, P. (2010). A Novel Approach for Improving Off-Axis Pixel Performance of Terahertz Focal Plane Arrays. *IEEE Transactions on Microwave Theory and Techniques*, *58*(7), 2014-2021.

Trichopoulos, G., & Sertel, K. (2015). Broadband Terahertz Computed Tomography Using a 5k-pixel Real-time THz Camera. Journal of Infrared, Millimeter, and Terahertz Waves, 36(7), 675-686.

Tripathi, S. R., Miyata, E., Ishai, P. B., & Kawase, K. (2015). Morphology of human sweat ducts observed by optical coherence tomography and their frequency of resonance in the terahertz frequency region. Scientific Reports, 5(1).

Wadell, B. C. (2003). Transmission line design handbook. Boston: Artech House.
Waller, J. C. (2002). Suspect identities: A history of criminal identification and fingerprinting. Journal of the History of the Behavioral Sciences, 38(4), 419-420.

Xiang-Xin, Z.; Chun-Ge, L. The Historical Application of Hand Prints in Chinese Litigation. J. Forensic Ident. 1988, 38 (6), 277–284.